Melilite-bearing lavas in Mayotte (France): An insight into the mantle source below the Comores

Anne-Aziliz Pelleter, Martial Caroff, Carole Cordier, Patrick Bachèlery, Pierre Nehlig, Delphine Debeuf, Nicolas Arnaud

Melilite-bearing lavas in Mayotte (France): an insight into the mantle source below the Comores

Anne-Aziliz Pelleter [a,1], Martial Caroff [a,*], Carole Cordier [b, c], Patrick Bachelery [d], Pierre Nehlig [e], Delphine Debeuf [f], Nicolas Arnaud [g]

[a] UMR CNRS n°6538 « Domaines Océaniques », Institut Universitaire Européen de la Mer, Université de Brest, 6 avenue Victor Le Gorgeu, CS 93837, F-29238 Brest Cédex 3, France

[b] Université Grenoble Alpes, ISTerre, F-38000 Grenoble, France

[c] CNRS, ISTerre, F-38041 Grenoble, France

[d] Laboratoire Magmas et Volcans, UMR n°6524 CNRS-IRD-Université Blaise Pascal, Observatoire de Physique du Globe de Clermont-Ferrand, 5, rue Kessler, F-63038 Clermont-Ferrand Cédex, France

[e] Bureau de Recherches Géologiques et Minières, 3, avenue Claude-Guillemin, BP 36009, F-45060 Orléans Cédex 2, France

[f] Laboratoire GéoSciences Réunion, Faculté des Sciences et Technologies, 15, avenue René Cassin, CS 92003, F-97744 Saint-Denis Cédex 9, La Réunion, France

[g] Géosciences Montpellier, UMR 5243, CC 60, Université Montpellier 2, Place E. Bataillon, F-34095 Montpellier Cédex 5, France

* Corresponding author: caroff@univ-brest.fr

[1] Present address : UMR CNRS n°7327, Institut des Sciences de la Terre d'Orléans, Université d'Orléans, 1A rue de la Férolerie, 45071 Orléans, France (anne-aziliz.pelleter@univ-orleans.fr)

Keywords: Comores; ocean island basalts; olivine melilitite; HIMU; mantle heterogeneity; metasomatism

1. Introduction

Olivine melilitites are alkaline and ultracalcic basic igneous rocks rich in melilite, a calcic sorosilicate, and devoid of feldspar. They are thought to be produced by low degree of partial melting of a CO_2-rich mantle source in both continental and oceanic contexts (Gudfinnsson and Presnall, 2005; Dasgupta et al., 2007). In continental zones, they are found at or near rifting zones, often in association with carbonatites. In the African continent, (olivine) melilitites have been observed in Sahara (Dautria et al., 1992), East African Rift (Bailey et al., 2005; Dawson, 2012; Mattsson et al., 2013), South Africa (Rogers et al., 1992; Janney et al., 2002), and Madagascar (Melluso et al., 2011). In oceanic setting, the olivine melilitites are produced in intraplate volcanoes (Maaløe et al., 1992; Hoernle and Schmincke, 1993). They correspond generally to post-erosional, late units (Brey, 1978). In the vicinity of the Africa continent, olivine melilitites have been collected in Gran Canaria (Brey, 1978; Hoernle and Schmincke, 1993) and Cape Verde Islands (Brey, 1978). Several authors have highlighted the chemical resemblance, for incompatible trace element and isotopic ratios, between (olivine) melilitites and ocean island basalts (OIB), sometimes with a HIMU (or high μ, where $\mu = {}^{238}U/{}^{204}Pb$) affinity (Rogers et al., 1992; Wilson et al., 1995; Janney et al., 2002).

The Comores Archipelago, composed of four volcanic islands (Mayotte, Anjouan, Moheli, and Grande Comore) is located in the Mozambique Channel between the continental blocks of Africa and Madagascar (Fig. 1). The initial volcanism period of the oldest island – Mayotte – onto the ocean floor is estimated to be ca. 15-10 Ma (Nougier et al., 1986), whereas the Karthala volcano of Grande Comore (the youngest island) is still active.

The mantle beneath the Comores is probably metasomatized, with modal amphibole and/or phlogopite (Späth et al., 1996; Class and Goldstein, 1997). In fact, Coltorti et al. (1999) evidenced a CO_2-related cryptic metasomatism episode beneath Grande Comore. The origin of the Comores volcanism is attributed by Hajash and Armstrong (1972) and Emerick and Duncan (1982) to the upwelling of a mantle plume. Nougier et al. (1986) proposed that the Comorian magmas derive from the upper mantle, beneath an ocean-continent transitional crust structured by old and deep lithospheric fractures, which were reactivated during late Tertiary. Four Comores lavas – one sample from Moheli and the three analyzed samples from Anjouan (Reisberg et al., 1993; Späth et al., 1996; Salters and White, 1998) – have a more radiogenic Pb composition than the other Indian OIB. They display an isotopic signature close to that of the Atlantic islands near the western African coast, as Cape Verde and Canary Islands (Sushchevskaya et al., 2013).

The present study of Mayotte Island (Comores Archipelago), based on new petrological and geochemical data, reveals the coexistence of a large number of melilite-bearing (including olivine melilitites) and HIMU-like lavas (with $^{206}Pb/^{204}Pb > 20$). Mayotte Island is thus a good example for studying the genesis of melilite-bearing lavas and their relation with a specific mantle composition.

2. Geological setting

Mayotte is the oldest island of the Comores archipelago (Fig. 1), emplaced, while intraplate, in an active tectonic area. The present-day geography of the area is the consequence of the Permian-Trias Karoo NW-SE rifting, which resulted in the separation between Gondwana and Indian-Madagascan continental blocks (Malod et al., 1991; Piqué, 1999). The oceanic basins of Somalia and Mozambique opened during the Jurassic, while the

Madagascar Island drifted southwards along the Davie Ridge. The main part of the sedimentary products in the Mozambique Channel results from the erosion of the Davie Ridge surrected during an Eocene compression phase (Leclaire et al., 1989). Since the middle Miocene, the tectonic regime in the Mozambique Channel is dominated by E-NE–W-SW extension, also identified in the East African Rift and in Madagascar (Bertil and Regnoult, 1998; Piqué, 1999).

Although the volcano morphology in the Comores archipelago is rather consistent with a chronological progression of the volcanism northwestwards (freshest reliefs in Grande Comore; presence of a coral reef only in Mayotte and, to a less extend, in Moheli: Fig. 1), the K-Ar geochronological data of the archipelago suggest a more complex history (Fig. 1). With exception of Grande Comore, in which old lavas do not crop out, each island displays a Neogene volcanic activity (shield stage?) together with a more recent one. The oldest subaerial lavas of the archipelago are found in Mayotte, consistently with its eroded morphology and the presence of a large coral reef. Only one coarse-grained rock of Anjouan is older (11.1±0.5 Ma, Nougier et al., 1986), very different from the shield lavas (from 3.9±0.3 Ma to 1.5±0.2 Ma, Nougier et al., 1986). However, no dating is available for the rocks constituting the submarine flanks of the islands. It is therefore very difficult to reasonably establish, or not, a chronological progression of volcanism throughout the archipelago.

Mayotte is located 300 km westward of Madagascar and 70 km southwestward of Anjouan (Fig. 1). It is constituted of two main volcanic islands (Grande Terre and Petite Terre: 348 km^2 and 16 km^2 in surface, respectively) and around twenty islets, within a lagoon of 1100 km^2 bordered by a 160 km-long coral reef (Fig. 2a). Grande Terre is a north-south lengthened island, culminating at 660 m (Bénara Mount). The emerged reliefs correspond to the superstructure of two coalescent eroded shield volcanoes, subsiding for 1.5 Ma (Debeuf,

2004; Nehlig et al., 2013). Petite Terre is a 5 km-long island located 4 km eastward of Grande Terre (Fig. 2d).

3. Sampling and analytical techniques

3.1. Sampling

The rocks presented here were collected during three field trips, in 2001 (sampling: D. Debeuf and P. Bachelery), 2010 and 2011 (sampling: P. Nehlig, F. Lacquement, and J. Bernard, with the financial and logistic support of the French BRGM).

Mayotte Island is characterized by an intense lateritic weathering and an important plant cover. Consequently, the main part of the volcanic substratum cannot be sampled. Although only the freshest rocks have been collected, a residual meteoric alteration induces relatively high loss on ignition (LOI) values in several samples. As all the samples having a LOI > 4.6 wt.% are affected by significant argillaceous / hydroxidic alteration, we have rejected them for the geochemical study.

Among about a hundred of samples collected in 2001, 24 lavas have been dated; 51 samples have been analyzed for major and trace elements, 17 for $^{87}Sr/^{86}Sr$, 23 for $^{143}Nd/^{144}Nd$ isotopes, and 8 for Pb isotopes. Among the 35 samples collected in 2010 and 2011: 19 samples have been analyzed for major and trace elements, 10 for $^{87}Sr/^{86}Sr$ isotopes, and 14 for Nd and Pb isotopes. A selection of geochronological and chemical data is shown in Tables 1, 2, and 3. The complete dataset is given in the supplementary Table S1.

3.2. $^{40}Ar/^{39}Ar$ datations

Bulk rock samples (flows, dykes and domes) were dated by the $^{40}Ar/^{39}Ar$ method. Analyses were performed on the 150- 250 µm-size groundmass fraction. For each sample, one or more aliquots on different separates (typically feldspar and volcanic glass) were irradiated on January 2002 at the McMaster reactor, Ontario, in the 5C position for 26 h under a 10^{18} neutrons $cm^{-2}s^{-1}$ flux. The irradiation standard is a Fish Canyon sanidine standard with an age of 28.02 ± 0.16 Ma (Renne et al., 1998), with reproductive values within 0.6%.

Ages were obtained at the University of Montpellier 2, following a protocol similar to that described in Arnaud et al. (2003) and Garcia et al. (2003). Details on the analytical conditions are available from the authors upon request. Age given from age spectra are weighted mean plateaus (Fleck et al., 1977) or simple mean ages. The latter case corresponds to the situation where either subsequent steps overlap only at the 1σ level or total ^{39}Ar cumulated from these steps is insufficient to define a classical plateau. All errors from age spectra take the error on the J factor into account. Plateau criterions being rarely achieved, sometimes simple mean age is given. The isochron ages are obtained in an inverse isochron diagram of $^{36}Ar/^{40}Ar$ versus $^{39}Ar/^{40}Ar$ (Roddick et al., 1980), which allows homogeneous excess components to be individualized in many occasions. Errors on age and intercept age include individual errors on each point and linear regression by York's method (York, 1969). The goodness of it relative to individual errors is measured by Mean Square Weighted Deviation (MSWD).

3.3. Mineral and whole rock analyses

Mineral compositions have been determined using a Cameca SX-100 electron microprobe (Microsonde Ouest, Brest, France) with an acceleration voltage of 15 kV and a beam current of 20 nA. Some high precision analyses of olivine were acquired using a JEOL

JXA-8230 electron microprobe (ISTerre, Grenoble, France) with an acceleration voltage of 25 kV and a beam current of 900 nA.

Major and trace element analyses for the rocks sampled in 2001 were determined at the CRPG (Centre de Recherches Pétrographiques et Géochimiques, Nancy, France), whereas samples collected in 2010-2011 were analyzed at the PSO/IUEM (Pôle Spectrométrie Océan, Institut Universitaire Européen de la Mer, Brest, France). Whole-rock major elements were analyzed by inductively coupled plasma atomic emission spectrometry (ICP-AES) following the analytical method described by Cotten et al. (1995). Relative standard deviations are < 2% (< 1% for SiO_2). Whole-rock trace elements were analyzed by inductively coupled plasma mass spectrometry (ICP-MS) following the sample preparation and analysis method of Barrat et al. (1996). Relative standard deviations are < 5% for most of the trace elements and < 10% for Nb, Gd, Tb, Ta, Ni, Zn and Rb. The concentrations found in the Mayotte OIB are well above the detection limits for all the trace elements analyzed.

Sr and some Nd isotopic ratios were measured by thermal ionization mass spectrometry (TIMS, Laboratoire Magmas et Volcans, Clermont-Ferrand, France and PSO/IUEM/IFREMER, Brest, France), while Pb and some Nd isotopic ratios were measured on a multicollector ICP-MS (PSO/IFREMER, Brest, France). Samples were leached in 2N HCl for about one hour and rinsed three times in ultrapure water to remove weathering effect. The protocol for element separation is described in Chauvel et al. (2011). Measured blanks are lower than 20 picograms (pg) for Nd, 60 pg for Sr and 100 pg for Pb (except one analysis session with 300 pg blank). Values used for mass fractionation corrections and relative standard deviations are given in Table 3.

4. Geochronology of Mayotte

Four volcanic domains have been recognized on Mayotte Island from geological and geomorphological observations, ages available in the literature (Hajash and Armstrong, 1972; Emerick and Duncan, 1982; Nougier et al, 1986; McDougall unpublished in Debeuf, 2004), and new $^{40}Ar/^{39}Ar$ ages obtained on 24 samples (Table 1).

The most eroded – and thus oldest – area is the southern part of the main island (Fig. 2b), where the hydrographic network is intensely erosive and most headlands correspond to inverted reliefs. The main building volcanic phase (> 10.6-~3.0 Ma) is mainly formed by alkali basalt, basanite and olivine nephelinite lava flows (Fig. 2c), strongly weathered to lateritic products. This phase ended with the intrusion of around fifteen phonolitic protrusions, associated with nephelinitic/phonolitic lava flows and pyroclastic density currents (3.9-3.1 Ma). The post-shield phase began with the emplacement of the tephriphonolitic/phonolitic Combani massif circa 2.4 Ma ago. The last events in the south domain are emission of pyroxene-bearing basanitic and nephelinitic lava flows (ca. 2.0-~1.5 Ma).

The northwest domain is characterized by sharp reliefs of moderately weathered basaltic-basanitic lava flow piles, contemporaneous to the southern main building phase (> 7.1-~4.0 Ma). These lavas constitute a second shield volcano, which would have emerged after the southern one (Stieljes, 1988). Lavas are cut by a basaltic intrusive network (sills and N–S-trending dykes). This volcanism was followed by an extension-related mafic magmatism, at about ~4.0-< 1.0 Ma, which renewed the reliefs. The two melilititic lava flows were probably emplaced during this event. Phonolitic domes (3.3 and 2.5 Ma) are especially rare (Fig. 2c).

The north central sector of Grande Terre is characterized by the least eroded, youngest reliefs (Fig. 2b). This is consistent with lava ages mainly comprised between 2.4 and 0.8 Ma, i.e. more recent than in both south and northwest domains. Two older samples have been dated at 3.4 Ma (Hajash and Armstrong, 1972) and 3.35 Ma (Emerick and Duncan, 1982), but

they have not been analyzed for major and trace elements. From west to east, the north central sector is composed of: (1) the Digo massif, made of basaltic-tephritic lava flows; and (2) the Mtsapéré stratovolcano (basaltic-tephritic lava flows intruded by phonolitic protrusions, Fig. 2c), lying on the northwest shield formations.

The fourth volcanic zone is a recent explosive complex comprising small pyroclastic edifices (tuff rings and cones) built by phreatomagmatism and strombolian eruptions along the east coast of Grande Terre and in Petite Terre (Fig. 2c). The activity is estimated from 500 000 to 150 000 years in Grande Terre and up to 4 000 years in Petite Terre, where the volcanic edifices lay on a Holocene barrier reef younger than 9000 years (Camoin et al., 2004). The subaerial explosive volcanoes lay on lateritized lava flows in Grande Terre. The first strombolian phase built edifices with interbedded lava flows and pyroclastic levels (scoriaceous blocks and lapilli, and ash). Then, the volcanism became phreatoplinian, with pumice-bearing tuff ring structures. Two of them crop out in Grande Terre and four in Petite Terre (three in the eastern part and a fourth in the southernmost area, Fig. 2c).

5. Petrology

5.1. Lavas and hypabyssal rocks

The mineral assemblage of the studied lavas is presented in Fig. 3. The petrographic nomenclature is based on mineralogy, total alkali-silica (TAS) and basanite-nephelinite-melilitite classification schemes of Le Bas et al. (1986) and Le Bas (1989), respectively (Figs. 4 and 5).

Most of the lava flows of south and northwest domains are alkali basalts and basanites. Lavas are usually porphyritic, sometimes cumulative (> 35 vol.% phenocrysts), with

clinopyroxene and/or olivine (Fo_{79-85}) phenocrysts. Groundmass generally has a microlitic texture. It is constituted of clinopyroxene (fassaite-diopside), olivine (Fo_{62-81}), plagioclase (An_{47-64}), nepheline, Fe-Ti oxides and apatite. Perovskite crystals have been identified as inclusions in clinopyroxene phenocrysts of one basanite from the south domain.

Two olivine melilitite lavas were collected near Mtsangamouji in the northwest domain. They are porphyritic with zoned olivine phenocrysts (Fo_{84-88}) immersed in a microlitic groundmass constituted of melilite, olivine (Fo_{79-84}), titanomagnetite, apatite, clinopyroxene, and tiny nepheline. One sample displays mingling features.

Olivine-free and olivine-bearing nephelinites occur as lava flows or dykes in the south domain and in a few areas of the northwest domain. They have a porphyritic texture with phenocrysts of clinopyroxene (fassaite-diopside) and nepheline. Groundmass crystals include nepheline, clinopyroxene, Fe-Ti oxides, and apatite. Olivine phenocrysts (Fo_{74-87}) and microcrysts (Fo_{69-78}) are only present in the olivine nephelinites, whereas hornblende, aegirine-augite, perovskite and titanite are detected only in olivine-free nephelinites. Microcrystals of melilite (< 10 vol.%) have been identified in two olivine nephelinites (PN2 and PN12f).

Tephritic and tephriphonolitic lavas occur in the south and north central domains. They have a porphyric fluidal microlitic texture. Phenocrysts are zoned augite and kaersutite, whereas groundmass includes plagioclase, clinopyroxene, Fe-Ti oxides, hastingsite and apatite. Tephriphonolites can be distinguished from tephrites by the presence of both K-feldspar as phenocrysts and arfvedsonite and aegirine-augite as microcrysts.

Phonolites occur as protusions or as derived lava flows, mainly in the south and north central domains and, sparsely, in the northwest one. They have a porphyritic microlitic texture, sometimes fluidal. Diopside, hornblende, K-feldspar, nepheline, and apatite occur as

phenocrysts and microcrysts. Moreover, the groundmass contains titanite, aegirine-augite, ferro-arfvedsonite, ferro-eckermannite and Fe-Ti oxides.

5.2. Pyroclastites and cumulates

Two types of pyroclastic formations have been identified: stombolian and phreatoplinian deposits, mainly located in the most recent domains of Mayotte (NE coast of Grande Terre and Petite Terre), and only sparsely represented in the older north central and south domains (Fig. 2c). Elements of the primary pyroclastic breccias are locally reworked as volcanogenic sedimentary deposits.

The strombolian edifices are small reddened scoria cones, composed of basaltic indurated lapilli- and bomb-sized fragments alternating with lava flows and ash levels. Locally, blocks of sedimentary rock (sandstone, arkose) are embedded in the breccias. The fragments bear iddingsitized olivine, pyroxene, nepheline and Fe-Ti oxides.

The phreatoplinian deposits are constituted of meter-sized interbedded sequences of pumice levels and hyaloclastite layers. Pumices range in size from 5 to 50 cm. They have a vesicular hyaloporphyric texture, with euhedral phenocrysts of K-feldspar, hornblende, and Fe-Ti oxides. Among the xenoliths, fragments of coral, lavas and scoria, dunitic and pyroxenitic cumulates are present. The basanitic xenolith PN5b, cumulative in olivine and clinopyroxene, has been found in the pumice sample PN5a.

Cumulates have been collected as xenoliths or blocks. They are dunites, pyroxenites, essexites and ijolites.

6. Geochemistry

6.1. Major elements

The subsequent geochemical study focuses on lavas and hypabyssal rocks (dykes and protrusions) of Grande Terre, together with pumices of Petite Terre. Major and trace element compositions of representative samples from Mayotte are listed in Table 2. The TAS diagram of Le Bas et al. (1986) (Fig. 4) can be used to evidence a large alkaline association in Mayotte from alkali basalts (only four analyzed samples), basanites and foidites to phonolites through intermediate lavas. Two trends are observed (Fig. 4): the first one, including mainly the south lavas, one basalt apart (M41), is highly silica-undersaturated; the second one, including the rocks from the three other domains, is moderately silica-undersaturated. Mafic rocks (MgO > 5 wt.%) are divided into three groups on the basis of silica-undersaturation, alkalinity and calcium content: basalts/basanites, olivine nephelinites and olivine melilitites (Fig. 5). Most of the nephelinites and olivine melilitites are gathered in the foidite field in the TAS diagram (Fig. 4). In general, silica-undersaturation increases from north central lavas to south shield lavas through northwest shield lavas (Fig. 4). Eleven olivine nephelinites and the two olivine melilitites contain CIPW normative larnite ($_N$larnite: Ca_2SiO_4), with contents higher than 10 % normative for olivine melilitites (Fig. 5), consistently with the criterion proposed by Wooley et al. (1996) to define this type of lavas. According to Médard et al. (2004), olivine melilitites can be considered as ultracalcic lavas (CaO > 13.5 wt.% and CaO/Al_2O_3 > 1 wt.%).

Plots of CaO, Al_2O_3, K_2O, and P_2O_5 against MgO are shown in figure 6. CaO is positively correlated with MgO for lavas with MgO < 8 wt%. The $_N$larnite samples and the mafic xenolith PN5b of Petite Terre have the highest CaO contents (> 12 wt. %). The (tephri)phonolites of the Combani massif form a low-CaO trend together with the lavas of the north central zone. Al_2O_3 and K_2O display remarkable negative correlations with MgO.

Except for the P_2O_5-rich $_N$larnite-bearing lavas, P_2O_5 increases with decreasing MgO up to MgO ~ 5 wt.%, then decreases.

6.2. Trace elements

We investigate in Figs. 6e-h the chemical distinction of the volcanic domains using incompatible trace element variations against Th.

(1) The post-shield lavas of the north central domain form linear trends versus Th. They are distributed in two groups with different Th concentrations and variable contents on Nb, Hf, and Yb. These samples have the lowest Nb/Zr ratios of the collection, displaying a decreasing trend with increasing Th.

(2) The recent phonolitic pumices of Petite Terre have the highest Nb, Hf, and Yb contents. Their Nb/Zr values range from 0.25 to 0.27.

(3) Most of the south domain samples plot linearly on the trace variation diagrams. Most of the corresponding lavas are contemporaneous with the shield phase. The trend has a slope especially low in the Hf versus Th diagram of figure 6f. The south domain samples are scattered in the Nb/Zr versus Th diagram of figure 6h.

(4) Amongst the south domain samples, the figure 6 diagrams can be used to discriminate four lavas, all of them located in the post-shield Combani massif. They plot apart in both Nb and Hf vs. Th diagrams (Fig. 6e and f), together with the Petite Terre pumices,.

(5) The northwest domain, mainly constituted of shield mafic lavas, cannot be easily distinguished in the figure 6 trace diagrams. The corresponding lavas plot either in the north central trend (Fig. 6a and f) or with the southern samples (Fig. 6e and g). Post-shield olivine melilitites M66 and FL386, presented above, belong to this domain.

Mafic samples (alkali basalts, basanites, olivine nephelinites and olivine melilitites) from Mayotte are enriched in light and middle REE (LREE and MREE, respectively) with respect to heavy REE (HREE), consistently with their OIB characteristics (Fig. 7a). Slope of the REE patterns increases from basalts/basanites to olivine nephelinites and to olivine melilitites. These latter are also slightly more enriched in middle MREE. In the primitive mantle-normalized multi-element diagram (Fig. 7b), patterns of the mafic lavas are bell shaped, as expected for OIB, and show strong negative anomalies in Rb, K and Pb, and, to a lesser extent, in U and Ti. Olivine melititites – especially FL 386 – display high values in U, Sr, P, Nd, Sm, Eu and Gd. Olivine-free nephelinites have, on average, higher REE contents than the mafic rocks (Fig. 7c). Phonolites have characteristic concave-up REE patterns, with low MREE values, and LREE and HREE compositions close to those of mafic and intermediate rocks. The pumices of Petite Terre, which have the highest REE contents amongst the phonolites, show a negative anomaly in Eu. Olivine-free nephelinites and all evolved rocks display negative anomalies in P and Ti (Fig. 7d). Moreover, phonolites (lavas and pumices) are depleted in Ba and phonolitic pumices also in Sr.

6.3. Isotopes

A selection of Sr and Nd isotopic ratios and all the Pb data are given in Table 3. In the $^{207}Pb/^{204}Pb$ vs. $^{206}Pb/^{204}Pb$ diagram of Figure 8a, there are evident relationships between the isotopic compositions of the samples and their geographic location and age. In fact, most of the lavas from the south and northwest shield volcanoes exhibit the most radiogenic $^{207}Pb/^{204}Pb$ (> 15.64) and $^{206}Pb/^{204}Pb$ (> 19.87), whereas the post-shield north central domain lavas display the lowest ratios ($^{207}Pb/^{204}Pb$ < 15.6 and $^{206}Pb/^{204}Pb$ < 19.35). The post-shield Combani lavas, northwest olivine melititites, and Petite Terre samples (xenolith PN5b apart)

show isotope ratios between these two groups but closer to north central lavas. This isotopic distribution seems to roughly reflect the volcanological history of the island. In general, lavas showing the most radiogenic Pb ratios have been sampled in the oldest parts of the island (> 3.0 Ma), whereas the other samples belong to formations having an age < ~2.5 Ma. The only exceptions are the HIMU-flavored M25 and DMM-like M137 lavas, samples respectively dated to 2.0 and 5.0 Ma but for which no plateau age could be calculated (Table 1). There is also an uncertainty about the olivine melilitites (M66 and FL386), the age of which ranges from 4.0 to < 1.0 Ma. Even if the variations in the $^{143}Nd/^{144}Nd$ vs. $^{206}Pb/^{204}Pb$ diagram are less contrasted, similar trends can be observed. The $^{143}Nd/^{144}Nd$ ratios of the rocks from the shield volcanoes, highly radiogenic in Pb, are more scattered and in average lower than those of the other samples. The $^{87}Sr/^{86}Sr$ ratio is less discriminative (Table 3).

When compared to other Comores Islands and mantle end-member (Depleted MORB-Mantle: DMM; high $^{238}U/^{204}Pb$: HIMU; Enriched Mantle: EM1 and 2, of Zindler and Hart, 1986) isotope compositions, the most recent lavas from Mayotte tend towards the depleted mantle, such as all the lavas produced by the La Grille volcano in Grande Comore and two samples from Moheli. In contrast, samples collected in the south and northwest shield volcanoes have a clear HIMU affinity, such as one sample from Moheli and all the lavas from Anjouan that have been analyzed for Pb isotopes.

The south alkali basalt M41, that spatially belongs to south group but that shows less silica-undersaturated composition, displays a Sr-Nd composition close to that of the Karthala volcano in Grande Comore, which tends toward the EM end-members (Table 3): its $^{143}Nd/^{144}Nd$ ratio is low (0.51272) and its $^{87}Sr/^{86}Sr$ ratio especially high (0.70383). M41 is relatively fresh (LOI=1.1) and it has low Rb/Sr ratio (0.5) suggesting that its high $^{87}Sr/^{86}Sr$ ratio is a pristine characteristic. M41 sample has not been analyzed for Pb isotopes. As EM-

like composition is restricted to this sample in Mayotte, sampling date and location have been thoroughly checked and confirm the expression of EM mantle component in Mayotte.

6.4. Spatial and temporal distribution of the geochemical characteristics

The lavas from the main building phase of the shield volcanoes (south and northwest domains) have more radiogenic Pb compositions than the post-shield rocks (Combani massif, north central domains and Petite Terre).

Shield units

The lavas from the south shield are among the highest silica-undersaturated of the island (Fig. 4) including olivine-bearing and olivine-free nephelinites, basanites and phonolites. They have the highest CaO contents together with the northwestern melilitites (Fig. 6a), and include most of the $_{N}$larnite samples (Table 2). The south shield lavas have a HIMU affinity, with high Pb isotope ratios (Fig. 8).

Most of the analyzed samples from the northwest shield are moderately silica-undersaturated mafic lavas, mainly basanites, with characteristic low incompatible trace element contents. They show a HIMU affinity (Fig. 8). The basanitic xenolith PN5b from Petite Terre (Table 2) shares the trace and isotopic signature of the northwest shield lavas. These features suggest that this sample could correspond to a lava from the northwest shield substratum, extracted during an explosive event and incorporated within the pumices.

Post-shield units

The only olivine melilitites of Mayotte are emplaced in the northwest domain during a post-shield extensional phase.

The post-shield lavas from the north central domain are moderately silica-undersaturated. They follow linear evolutionary trends in major and trace element diagrams

from basalts/basanites to phonolites through tephrite/tephriphonolites (Fig. 6). All the petrological types have a similar isotopic composition (e.g., Nd isotope ratios ranging from 0.51288 to 0.51290, Fig. 8b). Such features suggest that chemical variations in north central lavas reflect differentiation processes from melts generated from a rather homogeneous mantle source, more depleted than for the other lavas.

The Combani evolved samples follow the highly silica-undersaturated trend in the TAS diagram (Fig. 4). They have, however, lower CaO with respect to highly silica-undersaturated intermediate and felsic lavas of the south domain (Fig. 6a). Both groups have also similar behavior in HREE vs. Th diagrams (Fig. 6g and Table 2), reflecting probably comparable modalities of crystal fractionation. However, the Combani lavas are close to those of the north central domain in Hf vs. Th (Fig. 6f) and they have specific high Nb contents (Fig. 6e). Amongst the post-shield lavas, they have the most radiogenic $^{206}Pb/^{204}Pb$ values (Fig. 8).

The pumices of Petite Terre are phonolitic in composition. They belong to the moderately silica-undersaturated trend in the TAS diagram (Fig. 4) and plot in a restricted area of the trace element diagrams (Fig. 6e-g), away from all the other Mayotte samples.

7. Discussion

7.1. Olivine melilitite genesis

The olivine melilitites are ultracalcic mafic lavas, characterized by high contents in CaO and MgO; high silica-undersaturation, with SiO_2 contents < 40 wt.% (Wilson et al., 1995); low values in Al_2O_3, and, to a lesser extent, alkalis; and straight slopes in chondrite-normalized REE diagrams (Brey, 1978; Rogers et al., 1992; Wilson et al., 1995). Based on such chemical features, Brey (1978) and Rogers et al. (1992) have proposed that melilititic

primary magmas are generated by very low degree of partial melting of a garnet- (and phlogopite-?) bearing CO_2-rich mantle source. Such low partial melting models for melilititic melts are consistent with the experimental works of Gudfinnsson and Presnall (2005). Wilson et al. (1995) and Melluso et al. (2011) have suggested that carbonates (probably dolomite) were involved in the melting process. From data of experimental petrology, Gudfinnsson and Presnall (2005) have positioned the field of the mantle at the origin of melilititic primary melts in the domain of garnet stability, in presence of CO_2, at pressures ranging from 3 and 4 GPa. Partial melting experiments of carbonated peridotite at 3 GPa generate melt compositions close to melilititic lavas (Hirose, 1997; Dasgupta et al., 2007), except for TiO_2 and FeO^T, lower in these experimental melts than in natural olivine melilitites. To account for their geochemistry, Dasgupta et al. (2006, 2007) propose as melting source a carbonated peridotite metasomatized by pyroxenitic melts.

Besides the wide range of geochemical features listed above, the olivine melilitites of Mayotte present specific characteristics, namely high P_2O_5 and Sr contents (Figs. 6d and 7b, and Table 2), and relative enrichments in MREE with respect to the other mafic rocks (Fig. 7a). The sole other mention of P-rich melilitites has been made by Bailey et al. (2005) for Ugandan rocks. In the figure 6d diagram, it is shown that all the $_N$larnite samples are enriched in P_2O_5. Consequently, to explore the melilititic character of the P-rich $_N$larnite lavas, we have reported them in the P_2O_5 vs. $CaO/(SiO_2+Al_2O_3)$ diagram of figure 9: the higher this ratio is, the more silica-undersaturated, CaO-rich and Al_2O_3-poor the rock is. The positive correlation demonstrates that a high P_2O_5 content is also a melilititic feature in Mayotte. The P_2O_5 enrichment of the $_N$larnite lavas (Figs. 6d and 9), together with the relatively high Sr and MREE contents of both olivine melilitites (Table 2 and Fig. 7), is consistent with the hypothesis of an apatite contribution in the genesis of these lavas. Apatite can be involved through two mechanisms: (1) melting at very low degree of apatite-bearing pyroxenite veins

in lithospheric metasomatized mantle (Foley, 1992); (2) assimilation of apatite-bearing veins during the ascent of primary melts formed at a greater depth (Bailey et al., 2005). Scenario (1), implying small melting degrees, is consistent with the high silica-undersaturation of the $_{N}$larnite lavas, especially olivine melilitites. Both models imply a metasomatism episode, in which CO_2-rich fluids or carbonatitic melts are probably involved (Hirschmann et al., 2003). This is consistent with the classic models of melilitite genesis (see references above) and with the occurrence in Grande Comore lavas of mantle xenoliths metasomatized by alkali-carbonatitic melt (Coltorti et al., 1999).

7.2. HIMU-flavored lavas

In order to minimize the effects of melt differentiation (crystallization, contamination) and to discuss the contribution of the mantle sources, this section focuses on relatively mafic lavas (MgO > 5 wt.%). As evidenced in Figure 8, the isotopic composition of Mayotte lavas is consistent with mixing between depleted mantle and HIMU components.

The HIMU-flavored mafic lavas, characterized by high Pb isotopic ratios, are reputed to be enriched in Nb and Ta and depleted in alkali/earth-alkali elements relative to the other incompatible trace elements (Dupuy et al., 1989; Willbold and Stracke, 2006). These features are noticeable in the HIMU-like olivine nephelinites collected in the south shield of Mayotte (Table 2 and Fig. 7b). Nevertheless, rocks from the northwest shield, which also have a clear HIMU isotopic signature, do not show these trace element features.

The HIMU mantle end-member is generally considered as the signature of a long-lived mantle reservoir (> 1 Ga). It has been ascribed to (1) a metasomatized mantle that has undergone a removal of Rb and Pb (Zindler and Hart, 1986) and/or an U enrichment through CO_2-rich fluids (Nakamura and Tatsumoto, 1988); (2) an ancient subduction-modified

oceanic lithosphere, depleted in LILE as the result of dehydration (White and Hofmann, 1982; Dupuy et al., 1989); or (3) combination of both models, i.e. a peridotite metasomatized with carbonated silicate melts, carbonatites derived from a recycled oceanic crust (Jackson and Dasgupta, 2008) or carbonated eclogites (Dasgupta et al, 2010). The fact that the lavas from the northwest shield are not enriched in Ta and Nb (Table 2) is not really consistent with the model (2).

In Mayotte, only the oldest rocks show a HIMU signature. Contrary to some Marquesas examples as Ua Pou (Duncan et al., 1986; Legendre et al., 2005) and Eiao (Caroff et al., 1995), where the HIMU-like lavas have distinct petrographic and geochemical features compared to the other rocks, here, the isotopic composition is disconnected from the silica-undersaturation and elemental (major and trace elements) composition of the lavas, which precludes any connection between source composition and partial melting modalities.

The isotopic composition of Mayotte lavas is consistent with a mixing between DMM and HIMU end-members (Fig. 8). This feature has already been stated for the Canary Archipelago by Gurenko et al. (2009) and Aulinas et al. (2010). However, the HIMU-like lavas in Gran Canaria correspond to a post-shield phase (Aulinas et al., 2010), unlike Mayotte. Isotopic data for Canaries and Mayotte are both consistent with the assumption of small-scale HIMU heterogeneities in a depleted mantle (see section 7.3).

We compare the Nd/Yb vs. SiO_2 and Nd/Yb vs. Nb/Zr diagrams (Fig. 10) and the isotopic ratios (Fig. 8) in order to discriminate source composition, apatite contribution and melting degree. Apatite contribution during a deep metasomatism episode increases Nb/Yb ratio at constant Nb/Zr ratio and SiO_2 content. Decrease of melting degree induces a decrease of SiO_2 content and an increase of Nd/Yb and Nb/Zr ratios. From the data distribution in Figure 10, $_N$larnite-bearing lavas would result from low partial melting degree of a metasomatized apatite-bearing mantle source, with ($_N$larnite-bearing nephelinites) or without

(olivine melilitites) HIMU affinity (Fig. 8). South and northwest shield lavas would derive from a similar HIMU-like mantle source (Fig. 8) and their elemental distinction results from increase of the partial melting degree from south to northwest lavas. North central post-shield lavas derive from a more depleted mantle (Fig. 8), through higher melting degrees than lavas of the main building stage (Fig. 10).

7.3. Genesis of Comores lavas

Two groups of mantle source models below Comores are proposed, which imply interactions between melt issued (1) from an EM1-HIMU heterogeneous plume and a DMM metasomatized lithosphere (Deniel, 1998); and (2) from a homogeneous plume with a dominant EM1 signature and a DMM-HIMU metasomatized lithosphere (Class and Goldstein, 1994, 1997; Späth et al., 1996; Class et al., 1998). In the latter models, the HIMU component would be introduced in the Comorian mantle reservoir through delamination or thermal erosion of a continental lithosphere during the Gondwana break-up. This group of models is consistent with the geographic position of the Comores Archipelago between two HIMU-bearing continental blocks: Africa and Madagascar (Bell and Tilton, 2001; Melluso et al., 2011).

Our data are rather consistent with the second type of models for the mantle source below Mayotte (Fig. 11): clear DMM-HIMU mixing and quasi absence of EM1 compositions (except M41, Table 3). During the main building stage, partial melting of a DMM-HIMU CO_2-metasomatized lithosphere produced the south and northwest shield melts, with lower partial melting degrees for the south lavas (Fig. 10). The melting processes occurred in the garnet stability field, as suggested by the presence of $_N$larnite-bearing ultracalcic melts (Brey and Green, 1977). During the post-shield phase, the more isotopically depleted homogeneous

north central melts were formed through higher melting degrees. The other post-shield rocks have Nd and Pb isotopic features intermediate between this north central group and the lavas of the main building phase (Fig. 8). The progressive increase of the depleted component influence through time (Fig. 8), especially for the north central rocks (Fig. 10), can be related to a lower proportion of HIMU component in the mantle source or to a progressive dilution of the melts issued from fusible and small-sized HIMU heterogeneities when melt productivity increases. However, HIMU-flavored northwest lavas are produced by similar melting degrees as the depleted north central lavas. We thus propose that the isotopic signature of the post-shield north central lavas is related to a high partial melting of a source where the HIMU component would have been partially consumed during the main building stage. The olivine melilitites would be generated from a source isotopically equivalent, but enriched in CO_2 and P_2O_5 (probably with modal dolomite ± apatite) and with a low degree of partial melting. The most plausible lithologies for generating the silica-undersatured primary melts of Mayotte lavas are carbonated garnet peridotite (Hirose, 1997; Dasgupta et al., 2007) and/or silica-deficient garnet pyroxenite/eclogite (Hirschmann et al., 2003, Dasgupta et al., 2010; Le Roux et al., 2011). Considering that the HIMU signature of the rocks is disconnected from partial melting modalities and that the Mayotte lavas, more or less fractionated, are not primary magmas, it would be difficult to go further in characterization of the source lithology.

The model of a depleted lithospheric mantle with HIMU small-scale heterogeneities can be extended to the other islands of the Comores archipelago. Indeed, the mixing trend DMM-HIMU is clear for Moheli, Anjouan and “La Grille”-type lavas from Grande Comore (Fig. 8). Nevertheless, the “Karthala”-type recent lavas from Grande Comore show a specific EM1 signature ($^{87}Sr/^{86}Sr > 0.70350$ and $^{143}Nd/^{144}Nd < 0.51275$). Class et al (1998) argued that the “Karthala”-type lavas result from mixtures between plume and lithosphere melts. Thus, we propose that Comores lavas are mainly generated by partial melting of a DMM-HIMU

547 CO_2-metasomatized lithospheric mantle. The EM1 Comorian mantle plume would just have a
548 thermal effect, except for the "Karthala"-type lavas – and for the Mayotte basalt M41,
549 exhibiting an equivalent Sr-Nd isotopic composition – which probably resulted from
550 plume/lithosphere interactions (Fig. 11).
551
552 **8. Concluding remarks**
553
554 The new set of geochronological and geochemical data presented in this study is used
555 to discuss the chemistry and the mineralogy of the mantle source below Mayotte. The two
556 main results are: (1) the characterization for the first time in the Comores of melilite-bearing
557 lavas, including two olivine melilitites; and (2) the clear evidence of a HIMU signature in the
558 shield lavas. Both features may or may not concern same samples.
559 Without doubt, the melting mantle source involved in the genesis of the Mayotte lavas
560 is chemically and mineralogically heterogeneous at small scale. The HIMU affinity could find
561 its origin in lithospheric components metasomatized by CO_2-rich fluids, whereas melilite-
562 bearing lavas would derive from partial melting at very low degree of a mantle source,
563 isotopically similar or not, bearing modal carbonate and apatite. Time-increasing partial
564 melting during the main building phase of the shield volcanoes would favor the expression in
565 the post-shield lavas of a more depleted mantle signature, as the consequence of the dilution
566 of the HIMU heterogeneities in the mantle, maybe coupled with their partial consumption
567 during the shield phase.
568 Petrological and geochemical data can thus be used to draw a composite picture of the
569 mantle below Mayotte, which probably changes with time. Regardless of what lavas are
570 concerned, the melting lithosphere below Mayotte presents a general characteristic feature,
571 which reconciles both isotopic and mineralogical data: it has undergone CO_2-metasomatism.

572

573 **Acknowledgements**

574 Field studies were conducted in 2001 with the financial support of the Conseil
575 Régional de La Réunion and the Laboratoire GéoSciences Réunion, and in 2010 and 2011
576 with the financial and logistic support of the BRGM (Bureau de Recherches Géologiques et
577 Minières) and with the participation of F. Lacquement and J. Bernard. ISterre is part of Labex
578 OSUG@2020 (ANR10 LABX56). The authors are grateful to J. Langlade and V. Batanova
579 (microprobe analyses), C. Bollinger (ICP-MS Brest), Ph. Nonnotte (TI-MS), C. Liorzou (ICP-
580 AES), Y. Germain (MC-ICP-MS Ifremer), and P. Tiffenbach (thin sections). Detailed and
581 constructive remarks by Drs Meritxell Aulinas and Hannes B. Mattsson helped us a lot to
582 improve the manuscript. We also thank Dr Nelson Eby for his editorial assistance.

583

584 **Appendix. Supplementary Table S1.**

585 Supplementary data to this article can be found online at doi:
586

587 **References**

588

589 Arnaud, N., Tapponnier, P., Roger, F., Brunel, M., Scharer, U., Wen, C. and Zhiqin, X., 2003.
590 Evidence for Mesozoic shear along the western Kunlun and Altyn-Tagh fault, northern
591 Tibet (China). Journal of Geophysical Research, 108(B1), 2053,
592 doi:10.1029/2001JB000904.
593 Audru, J.C., Guennoc, P., Thinon, I., Abellard, O., 2006. Bathymay: la structure sous-marine
594 de Mayotte révélée par l'imagerie multifaisceaux. Compte Rendus Geoscience 338,
595 1240-1249.

596 Aulinas, M., Gimeno, D., Fernandez-Turiel, J.L., Font, L., Perez-Torrado, F.J., Rodriguez-
597 Gonzalez, A., Nowell, G.M., 2010. Small-scale mantle heterogeneity on the source of
598 the Gran Canaria (Canary Islands) Pliocene-Quaternary magmas. Lithos 119, 377-392.
599 Barrat, J.-A., Keller, F., Amossé, J., Taylor, R.N., Nesbitt, R.W., Hirata, T., 1996.
600 Determination of rare earth elements in sixteen silicate reference samples by ICP-MS
601 after Tm addition and ion exchange separation. Geostandards Newsletters 20, 133-139.
602 Barrat, J.-A., Zanda, B., Moynier, F., Bollinger, C., Liorzou, C., Bayon, G., 2012.
603 Geochemistry of CI chondrites: Major and trace elements, and Cu and Zn isotopes.
604 Geochimica et Cosmochimica Acta 83, 79-92.
605 Bailey, K., Lloyd, F., Kearns, S., Stoppa, F., Eby, N., Woolley, A., 2005. Melilitite at Fort
606 Portal, Uganda. Another dimension of the carbonate volcanism. Lithos 85, 15-25.
607 Bell, K., Tilton, G.R., 2001. Nd, Pb and Sr isotopic compositions of East African
608 carbonatites: evidence for mantle mixing and plume inhomogeneity. Journal of
609 Petrology 42, 1927-1945.
610 Bertil, D., Regnoult, J.M., 1998. Seismotectonic of Madagascar. Tectonophysics 294, 57-74.
611 Brey, G., 1978. Origin of olivine melilitites – chemical and experimental constraints. Journal
612 of Volcanology and Geothermal Research 3, 61-88.
613 Brey, G., Green, D.H., 1977. Systematic study of liquidus phase relations in olivine melilitite
614 + H_2O + CO_2 at high pressures and petrogenesis of an olivine melilitite magma.
615 Contributions to Mineralogy and Petrology 61, 141-162.
616 Camoin, G.F., Montaggioni, L.F., Braithwaite, C.J.R., 2004. Late glacial to post glacial sea
617 levels in the Western Ocean. Marine Geology 206, 119–146.
618 Caroff, M., Maury, R.C., Vidal., Ph., Guille, G., Dupuy, C., Cotten, J., Guillou, H., Gillot, P.-
619 Y., 1995. Rapid temporal changes in Ocean Island Basalt composition: evidence from a
620 800 m-deep drill hole in Eiao shield (Marquesas). Journal of Petrology 36, 1333-1365.

621 Chauvel, C., Bureau, S., Poogi, C., 2011. Comprehensive chemical and isotopic analyses of
622 basalt and sediment reference materials. Geostandards and Geoanalytical Research. 35,
623 125-143.
624 Class, C., Goldstein, S.L., 1994. Ocean island basalts and lithospheric melting: constraints
625 from the source mineralogy. V.M. Goldschmidt Conference, Edimburgh, Abstr. Vol., p.
626 175.
627 Class, C., Goldstein, S.L., 1997. Plume-lithosphere interactions in the ocean basins:
628 constraints from the source mineralogy. Earth Planet. Sci. Lett. 150, 245-260.
629 Class, C., Goldstein, S.L., Altherr, R., Bachelery, P., 1998. The process of Plume -
630 Lithosphere interactions in the Ocean Basins - The case of Grande Comore. Journal of
631 Petrology 39, 881-903.
632 Class, C., Goldstein, S.L., Shirey, S.B., 2009. Osmium isotopes in Grande Comore lavas: a
633 new extreme among a spectrum of EM-type mantle endmembers. Earth and Planetary
634 Science Letters 284, 219-227.
635 Class, C., Goldstein, S.L., Stute, M., Kurz, M., Schlosser, P., 2005. Grande Comore island: a
636 well-constrained low 3He/4He mantle plume. Earth and Planetary Science Letters 233,
637 391-409.
638 Coltorti, M., Bonadiman, C., Hinton, R.W., Siena, F., Upton, B.G.J., 1999. Carbonatite
639 metasomatism of the oceanic upper mantle: evidence from clinopyroxenes and glasses
640 in ultramafic xenoliths of Grande Comore, Indian Ocean. Journal of Petrology 40, 133-
641 165.
642 Cotten, J., Le Dez, A., Bau, M., Caroff, M., Maury, R.C., Dulski, P., Fourcade, S., Bohn, M.,
643 Brousse, R., 1995. Origin of anomalous rare-earth elements and yttrium enrichments in
644 sub-aerially exposed basalts: evidence from French Polynesia. Chemical Geology 119,
645 115-138.

646 Dasgupta, R., Hirschmann, M.M., Smith, N.D., 2007. Partial melting experiments of
647 peridotite + CO_2 at 3 GPa and genesis of alkali ocean island basalts. Journal of
648 Petrology 48, 2093-2124.
649 Dasgupta, R., Jackson, M.G., Lee, C.-T.A., 2010. Major element chemistry of ocean island
650 basalts – Conditions of mantle melting and heterogeneity of mantle source. Earth and
651 Planetary Science Letters 289, 377-392.
652 Dasgupta, R., Hirschmann, M.M., Stalker, K., 2006. Immiscible transition from carbonate-
653 rich to silicate-rich melts in the 3 GPa melting interval of eclogite + CO_2 and genesis of
654 silica-undersaturated ocean island lavas. Journal of Petrology 47, 647-671.
655 Dautria, J.M., Dupuy, C., Takherist, D., Dostal, J., 1992. Carbonate metasomatism in the
656 lithospheric mantle: peridotitic xenoliths from a melilititic district of the Sahara basin.
657 Contributions to Mineralogy and Petrology 111, 37-52.
658 Dawson, J.B., 2012. Nephelinite-melilitite-carbonatite relationships: Evidence from
659 Pleistocene-recent volcanism in northern Tanzania. Lithos 152, 3-10.
660 Debeuf, D., 2004. Etude de l'évolution volcano-structurale et magmatique de Mayotte
661 (Archipel des Comores, Océan Indien). Thesis, University of La Réunion, 277 pp.
662 Deniel, 1998. Geochemical and isotopic (Sr, Nd, Pb) evidence for the plume-lithosphere
663 interactions in the genesis of Grande Comore magmas (Indian Ocean). Chemical
664 Geology 144, 281-303.
665 Duncan, R. A., McCulloch, M. T., Barsczus, H. G., Nelson, D. R., 1986. Plume vs
666 lithospheric melts at Ua Pou, Marquesas Islands. Nature 322, 534-538.
667 Dupré, B., Allègre, C.-J., 1983. Pb-Sr isotope variation in Indian Ocean basalts and mixing
668 phenomena. Nature 303, 142-146.

669 Dupuy, C., Barsczus, H.G., Dostal, J., Vidal, P., Liotard, J.M., 1989. Subducted and recycled
670 lithosphere as the mantle source of ocean island basalts from southern Polynesia, central
671 Pacific. Chemical Geology 77, 1-18.
672 Emerick, C.M., Duncan, R.A., 1982. Age progressive volcanism in the Comores Archipelago,
673 western Indian Ocean and implications for Somali plate tectonics. Earth and Planetary
674 Science Letters 60, 415-428.
675 Fleck, F.J., Sutter, J.F., Elliot, D.H., 1977. Interpretation of discordant $^{40}Ar/^{39}Ar$ age spectra
676 of Mesozoic tholeiites from Antarctica. Geochimica et Cosmochimica Acta, 41, 15-32.
677 Foley, S., 1992. Vein-plus-wall-rock melting mechanisms in the lithosphere and the origin of
678 potassic alkaline magmas. Lithos 28, 435-453.
679 Garcia, S., Arnaud, N.O., Angelier, J., Françoise, B., Homberg, C., 2003. Rift jump process in
680 northern Iceland since 10 Ma from $^{40}Ar/^{39}Ar$ geochronology. Earth and Planetary
681 Science Letters 214, 529–544.
682 Gudfinnsson, G.H., Presnall, D.C., 2005. Continuous gradiations among primary carbonatitic,
683 kimberlitic, melilititic, basaltic, picritic and komatiitic melts in equilibrium with garnet
684 lherzolite at 3-8 GPa. Journal of Petrology 46, 1645-1659.
685 Gurenko, A.A., Sobolev, A.V., Hoernle, K.A., Hauff, F., Schmincke, H.-U., 2009. Enriched,
686 HIMU-type peridotite and depleted recycled pyroxenite in the Canary plume: A mixed-
687 up mantle. Earth and Planetary Science Letters 277, 514-524.
688 Hajash, A., Armstrong, R.L., 1972. Paleomagnetic and radiometric evidence for the age of the
689 Comores Islands, West Central Indian Ocean. Earth and Planetary Science Letters 16,
690 231-236.
691 Hirschmann, M.M., Kogiso, T., Baker, M.B., Stolper, E.M., 2003. Alkalic magmas generated
692 by partial melting of garnet pyroxenite. Geology 31, 481-484.

693 Hirose, K., 1997.Partial melt compositions of carbonated peridotite at 3 GPa and role of CO_2
694 in alkali-basalt magma generation. Geophysical Research Letters 24 (22), 2837-2840.
695 Hoernle, K., Schmincke, H.-U., 1993. The petrology of the tholeiites through the melilite
696 nephelinites on Gran Canaria, Canary Islands: crystal fractionation, accumulation and
697 depths of melting. Journal of Petrology 34, 573-597.
698 Janney, P.E., Le Roex, A.P., Carlson, R.W., Viljoen, K.S., 2002. A chemical and multi-
699 isotope study of the Western Cape olivine melilitite province, South Africa: implications
700 for the sources of kimberlites and the origine of the HIMU signature in Africa. Journal
701 of Petrology 43, 2339-2370.
702 Jackson, M.G., Dasgupta, R., 2008. Compositions of HIMU, EM1 and EM2 from global
703 trends between radiogenic isotopes and major elements in ocean island basalts. Earth
704 and Planetary Science Letters 276, 175-186.
705 Le Bas, M.J., 1989. Nephelinitic and basanitic rocks. J. Petrol. 30, 1299-1313.
706 Le Bas, M.J., Le Maitre, R.W., Streckeisen, A., Zanettin, B., 1986. A chemical classification
707 of volcanic rocks based on the total alkali-silica diagram. Journal of Petrology 27, 745-
708 750.
709 Leclaire, L., Bassias, Y., Clocchiatti, M., Ségoufin, J., 1989. La ride de Davie dans le canal de
710 Mozambique : approche stratigraphique et géodynamique. Comptes Rendus de
711 l'Académie des Sciences, Paris 308, 1077-1089.
712 Legendre, C., Maury, R.C., Caroff, M., Guillou, H., Cotten, J., Chauvel, C., Bollinger, C.,
713 Hémond, C., Guille, G., Blais, S., Rossi, P., Savanier, D., 2005. Origin of exceptionally
714 abundant phonolites on Ua Pou Island (Marquesas, French Polynesia): Partial melting of
715 basanites followed by crustal contamination. Journal of Petrology 46, 1925-1962.

716 Le Roux, V., Dasgupta, R., Lee, C.-T.A., 2011. Mineralogical heterogeneities in the Earth's
717 mantle: Constraints from Mn, Co, Ni and Zn partitioning during partial melting. Earth
718 and Planetary Science Letters 307, 395-408.
719 Maaløe, S., James, D., Smedley, P., Petersen, S., Grarmann, L.B., 1992. The Koloa volcanic
720 suite of Kauai, Hawaii. Journal of Petrology 33, 761-784.
721 Malod, J.A., Mougenot, D., Raillard, S., Maillard, A., 1991. Nouvelles contraintes sur la
722 cinématique de Madagascar : les structures de la chaîne de Davie. Comptes Rendus de
723 l'Académie des Sciences, Paris 312, 211-214.
724 Mattsson, H.B., Nandedkar, R.H.., Ulmer, P., 2013. Petrogenesis of the melititic and
725 nephelinitic rock suites in the Lake Natron – Engaruka monogenetic volcanic field,
726 northern Tanzania. Lithos 179, 175-192.
727 McDonough, W.F., Sun, S.-S., 1995. The composition of the Earth. Chemical Geology 120,
728 223-253.
729 Médard, E., Schmidt, M.W., Schiano, P., 2004. Liquidus surfaces of ultracalcic primitive
730 melts: formation conditions and sources. Contributions to Mineralogy and Petrology
731 148, 201-215.
732 Melluso, L., Le Roex, A.P., Morra, V., 2011. Petrogenesis and Nd-, Pb-, Sr-isotope
733 geochemistry of the Cenozoïc olivine melilitites and olivine nephelinites ("ankaratrites")
734 in Madagascar. Lithos 127, 505-521.
735 Nakamura, Y., Tatsumoto, M., 1988. Pb, Nd and Sr isotopic evidence for a multi-component
736 source for rocks of the Cook-Austral Islands and heterogeneities of mantle plumes.
737 Geochimica et Cosmochimica Acta 52, 2909-2924.
738 Nehlig, P., Lacquement, F., Bernard, J., Caroff, M., Deparis, J., Jaouen, T., Pelleter, A.-A.,
739 Perrin, J., Prognon, C., Vittecoq, B., 2013. Notice de la carte géologique de Mayotte à
740 1/25 000, BRGM/RP-61803-FR. BRGM Éditions, Orléans.

741 Nougier, J., Cantagrel, J.-M., Karche, J.P., 1986. The Comores archipelago in the western
742 Indian Ocean: volcanology, geochronology and geodynamic setting. Journal of African
743 Earth Sciences 5, 135-145.
744 Piqué, A., 1999. L'évolution géologique de Madagascar et la dislocation du Gondwana : une
745 introduction. Journal of African Earth Sciences 28 (4), 919-930.
746 Reisberg, L., Zindler, A., Marcantonio, F., White, W., Wyman, D., Weaver, B., 1993. Os
747 isotope systematics in ocean island basalts. Earth and Planetary Science Letters 120,
748 149-167.
749 Renne, .R., Swisher, C.C., Deino, A.L., Karner, D.b., Owens, T.l., DePaolo, D.J., 1998.
750 Intercalibration of standards, absolute ages and uncertainities in Ar^{40}/Ar^{39} dating.
751 Chemical Geology 145, 117-152.
752 Roddick, J.C., Cliff, R.A., Rex, D.C., 1980. The evolution of excess argon in alpine biotites—
753 an ^{40}Ar–^{39}Ar analysis. Earth and Planetary Science Letters 48, 185–208.
754 Rogers, N.W., Hawkesworth, C.J., Palacz, Z.A., 1992. Phlogopite in the generation of
755 olivine-melilitites from Namaqualand, South Africa and implications for element
756 fractionation processes in the upper mantle. Lithos 28, 347-365.
757 Salters, V.J.M., White, W.M., 1998. Isotope constraints on mantle evolution. Chemical
758 Geology 145, 447-460.
759 Späth, A., Le Roex, A.P., Duncan, R.A., 1996. The geochemistry of lavas from the Comores
760 Archipelago, western Indian Ocean: petrogenesis and mantle source region
761 characteristics. Journal of Petrology 37 (4), 961-994.
762 Stieltjes, L., 1988. Notice explicative de la carte géologique de Mayotte à 1/50 000. BRGM
763 Éditions, Orléans.

764 Suschevskaya, N.M., Kamenetsky, V.S., Belyatsky, B.V., Artamonov, A.V., 2013.
765 Geochemical evolution of Indian Ocean basaltic magmatism. Geochemistry
766 International 51 (8), 599-622.
767 Tindle, A.G., Webb, P.C., 1994. Probe-Amph-A spreadsheet program to classify microprobe
768 derived amphibole analyses. Computer & Geosciences 20 (7/8), 1201-1228.
769 White, W.M., Hofmann, A.W., 1982. Sr and Nd isotope geochemistry of oceanic basalts and
770 mantle evolution. Nature 296, 821-825.
771 Willbold, M., Stracke, A., 2006. Trace element composition of mantle end-members :
772 Implications for recycling of oceanic and upper and lower continental crust.
773 Geochemistry Geophysics Geosystems 7, Q04004, doi : 10.1029/2005GC001005.
774 Wilson, M. Rosembaum, J.M., Dunworth, E.A., 1995. Melilitites: partial melts of the thermal
775 boundary layer? Contributions to Mineralogy and Petrology 119, 181-196.
776 Wooley, A.R. et al., 1996. Classification of lamprophyres, lamproites, kimberlites and th
777 kalsitic, melilitic and leucitic rocks. The Canadian Mineralogist 34, 175-186.
778 York, D., 1969. Least square fitting on a straight line with correlated errors, Earth and
779 Planetary Science Letters 5, 320-324.
780 Zindler, A., Hart, S., 1986. Chemical geodynamics. Annual Review of Earth and Planetary
781 Sciences 14, 493-571.
782 Zinke, J., Reijmer, J.J.G., Thomassin, B.A., 2003. Systems tracts sedimentology in the lagoon
783 of Mayotte associated with the Holocene transgression. Sedimentary Geology 160, 57-
784 79.

785

786 **Figure captions**

787

Fig. 1. The Comores archipelago. K-Ar age ranges are indicated for each island: Grande Comore (2 data by Hajash and Armstrong, 1972, and Emerick and Duncan, 1982); Moheli (12 data by Emerick and Duncan, 1982, and Nougier et al., 1986); Anjouan (8 data by Hajash and Armstrong, 1972, Emerick and Duncan, 1982, and Nougier et al., 1986); Mayotte (34 data by Hajash and Armstrong, 1972, Emerick and Duncan, 1982, and Nougier et al., 1986, and one relative age determined by Zinke et al., 2003, for a pumice layer interbedded in the lagoon stratigraphic succession). The value of 11.1 Ma of Anjouan corresponds to a remote value measured on a syenitic xenolith. The Mayotte new age range of Table 1 is indicated in italic. Inset: Mayotte in its geodynamical context.

Fig. 2. Geophysical and geological maps of Mayotte. (a) Bathymetry (from Audru et al., 2006). (b) Digital terrain model (DTM) of Mayotte (Nehlig et al., 2013); mounts: 1. Mlima Dziani Bolé (472 m); 2. Mlima Digo (255 m); 3. Mlima Mtsapéré (572 m); 4. Mlima Combani (477 m); 5. Mlima Bénara (660 m); 6. Mlima Choungui (594 m). (c) Geological sketch of Mayotte, based on Debeuf (2004) and Nehlig et al. (2013); the main four domains (south, northwest, north central, Petite Terre), limited by bold dashed lines, have been defined from topographic, geochronological, petrographic and geochemical criteria; M&I rocks: mafic and intermediate rocks; samples listed in Tables 1 and 2 are positioned. (d) Volcanological sketch of Petite Terre, showing tuff ring structures.

Fig. 3. Summary of petrographic data for Mayotte lavas: mineral occurrence and their compositional range. NC: north central domain; Fo: forsterite; Wo: wollastonite; En: enstatite; Ne: nepheline; An: anorthite; Or: orthoclase; Aegir.-augite: aegirine-augite; Fe-arfv.: ferro-arfvedsonite; Fe-ecker.: ferro-eckermannite. Nomenclature of amphiboles based on Tindle and Webb (1994).

Fig. 4. Total alkali-silica (TAS) discrimination diagram for lavas and pumices from Mayotte (weight percent). The fields are from Le Bas et al. (1986). For this diagram, major element values were recalculated to 100% in a free water basis. The Combani samples (south domain) are identified by a bold half circle.

Fig. 5. Nephelinite-melilitite-basanite classification diagram of Le Bas (1989) for mafic lavas (MgO > 5 wt.%) from Mayotte (weight percent). Inset: olivine melilitite-nephelinite discrimination diagram of Wooley et al. (1996), same samples. Symbols as in figure 4.

Fig. 6. Variation of CaO, Al_2O_3, K_2O and P_2O_5 vs. MgO (weight percent) and Nb, Hf, Yb and Nb/Zr vs. Th (ppm) for lavas and pumices from Mayotte. Symbols as in figure 4.

Fig. 7. Trace element patterns of representative Mayotte samples. (a) and (b): mafic lavas (MgO > 5 wt.%); (c) and (d): intermediate nephelinites and phonolites. (a) and (c): chondrite-normalized REE patterns (normalization values: Barrat et al., 2012); (b) and (d): primitive mantle-normalized incompatible trace element patterns (normalization values: McDonough and Sun, 1995).

Fig. 8. (a) $^{143}Nd/^{144}Nd$ vs. $^{206}Pb/^{204}Pb$ and (b) $^{207}Pb/^{204}Pb$ vs. $^{206}Pb/^{204}Pb$ isotope diagrams showing Mayotte data compared with previously published data (Grande Comore: Dupré and Allègre, 1983; Reisberg et al., 1993; Späth et al., 1996; Class and Goldstein, 1997; Class et al., 1998; Deniel, 1998; Class et al., 2005; Class et al., 2009; Anjouan: Reisberg et al, 1993; Salters and White, 1998; Moheli: Reisberg et al., 1993; Späth et al., 1996). The position of the

837 DMM, EM I and II, and HIMU end-members are from Zindler and Hart (1986). Symbols as
838 in figure 4.
839
840 Fig. 9. P_2O_5 vs. CaO/SiO_2 (wt. %) diagram for the $_N$larnite lavas. Symbols as in figure 4.
841
842 Fig. 10. (a) Nd/Yb (ppm) vs. SiO_2 (wt. %) and (b) Nd/Yb vs. Nb/Zr (ppm) diagrams for the
843 basic lavas from Mayotte. PM: partial melting. The grey areas correspond to HIMU-flavored
844 lava samples ($^{206}Pb/^{204}Pb > 19.87$).
845
846 Fig. 11. Schematic model showing the mantle structure below Mayotte during its main
847 building phase. Partial melting of a DMM-HIMU CO_2-metasomatized lithosphere produced
848 the south and northwest shield melts, with lower partial melting degrees for the south lavas.
849 The melting processes occurred in the garnet stability field.
850

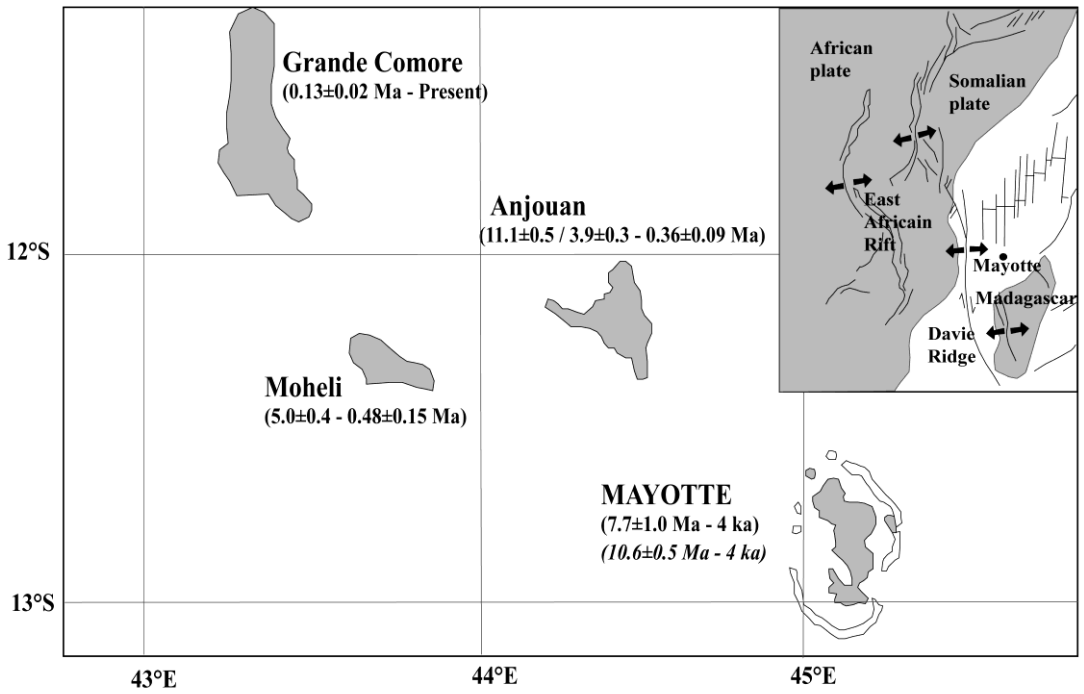

Pelleter et al. Fig. 1

851

852

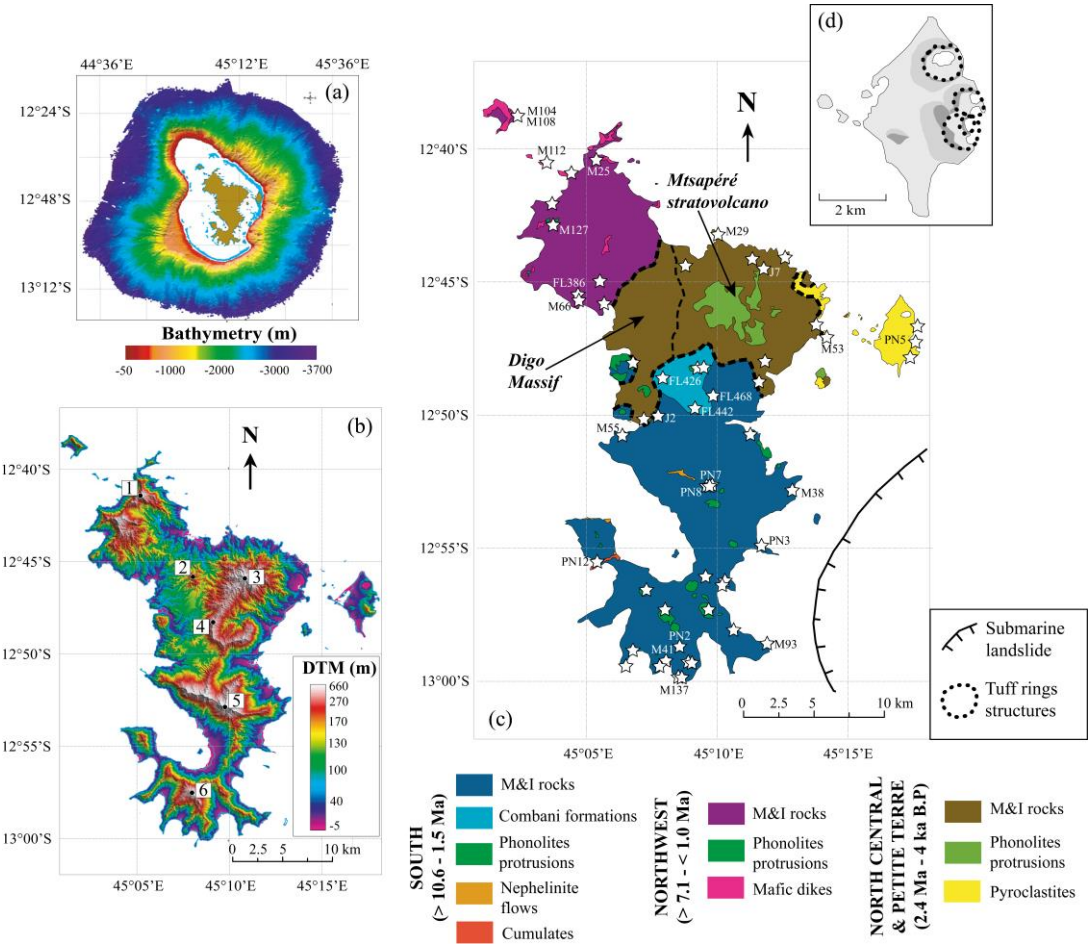
(a)
44°36'E
45°12'E
45°36'E
12°24'S
12°48'S
13°12'S
Bathymetry (m)
-50 -1000 -2000 -3000 -3700
(b)
N
DTM (m)
660
270
170
130
100
40
-5
0 2.5 5 10 km
12°40'S
12°45'S
12°50'S
12°55'S
13°00'S
45°05'E
45°10'E
45°15'E
1
2
3
4
5
6
(c)
N
Mtsapéré stratovolcano
Digo Massif
M104
M108
M112
M25
M127
FL386
M66
M29
J7
M53
PN5
FL426
FL468
FL442
J2
M55
PN7
PN8
M38
PN3
PN12
PN2
M41
M93
M137
0 2.5 5 10 km
(d)
2 km
Submarine landslide
Tuff rings structures
SOUTH (> 10.6 - 1.5 Ma)
M&I rocks
Combani formations
Phonolites protrusions
Nephelinite flows
Cumulates
NORTHWEST (> 7.1 - < 1.0 Ma)
M&I rocks
Phonolites protrusions
Mafic dikes
NORTH CENTRAL & PETITE TERRE (2.4 Ma - 4 ka B.P)
M&I rocks
Phonolites protrusions
Pyroclastites

853

854 Fig. 2

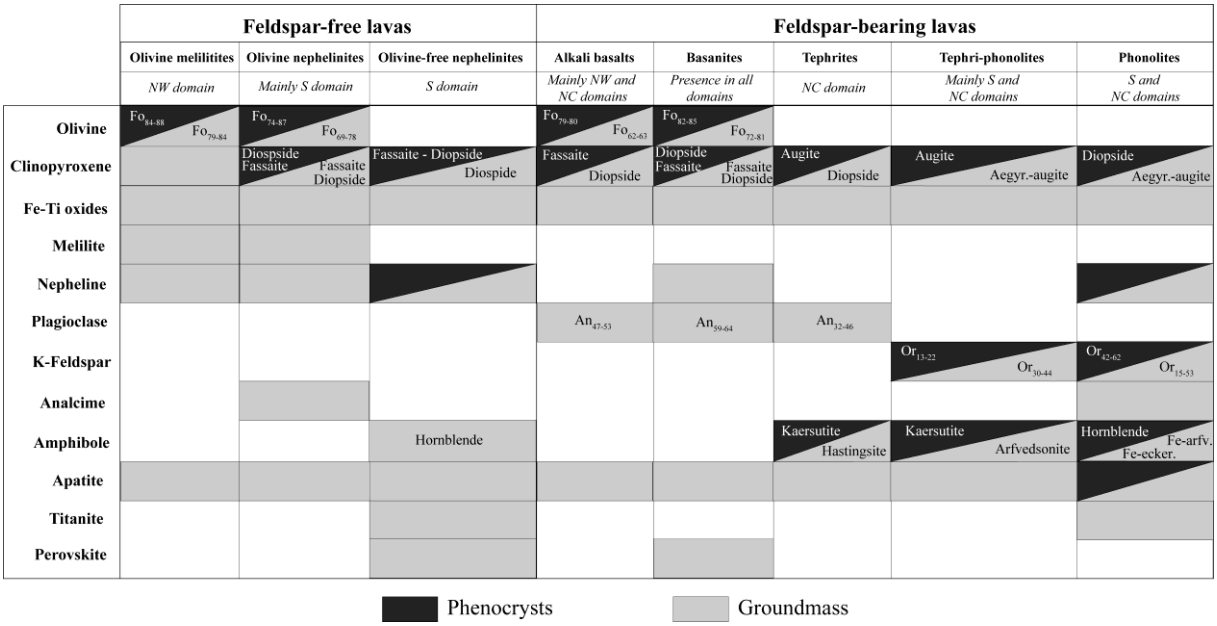
Feldspar-free lavas
Feldspar-bearing lavas
Olivine melilitites
Olivine nephelinites
Olivine-free nephelinites
Alkali basalts
Basanites
Tephrites
Tephri-phonolites
Phonolites
NW domain
Mainly S domain
S domain
Mainly NW and NC domains
Presence in all domains
NC domain
Mainly S and NC domains
S and NC domains
Olivine
Clinopyroxene
Fe-Ti oxides
Melilite
Nepheline
Plagioclase
K-Feldspar
Analcime
Amphibole
Apatite
Titanite
Perovskite
Fo84-88
Fo79-84
Fo74-87
Fo69-78
Fo79-80
Fo62-63
Fo82-85
Fo72-81
Diospside
Fassaite
Fassaite
Diopside
Fassaite - Diopside
Diopside
Fassaite
Diopside
Diopside
Fassaite
Fassaite
Diopside
Augite
Diopside
Augite
Aegyr.-augite
Diopside
Aegyr.-augite
An47-53
An59-64
An32-46
Or13-22
Or30-44
Or42-62
Or15-53
Hornblende
Kaersutite
Hastingsite
Kaersutite
Arfvedsonite
Hornblende
Fe-arfv.
Fe-ecker.
Phenocrysts
Groundmass

855

856 Fig. 3

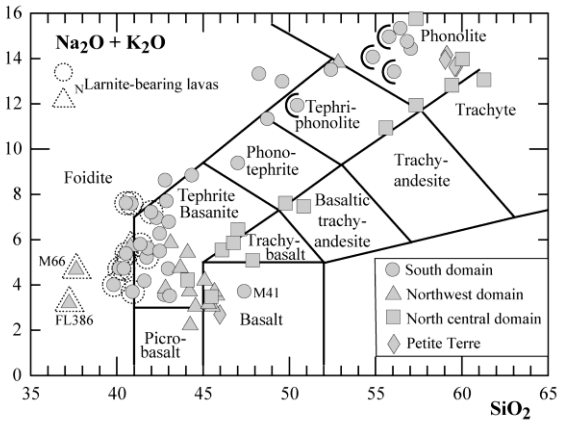

857

858

859 Fig. 4

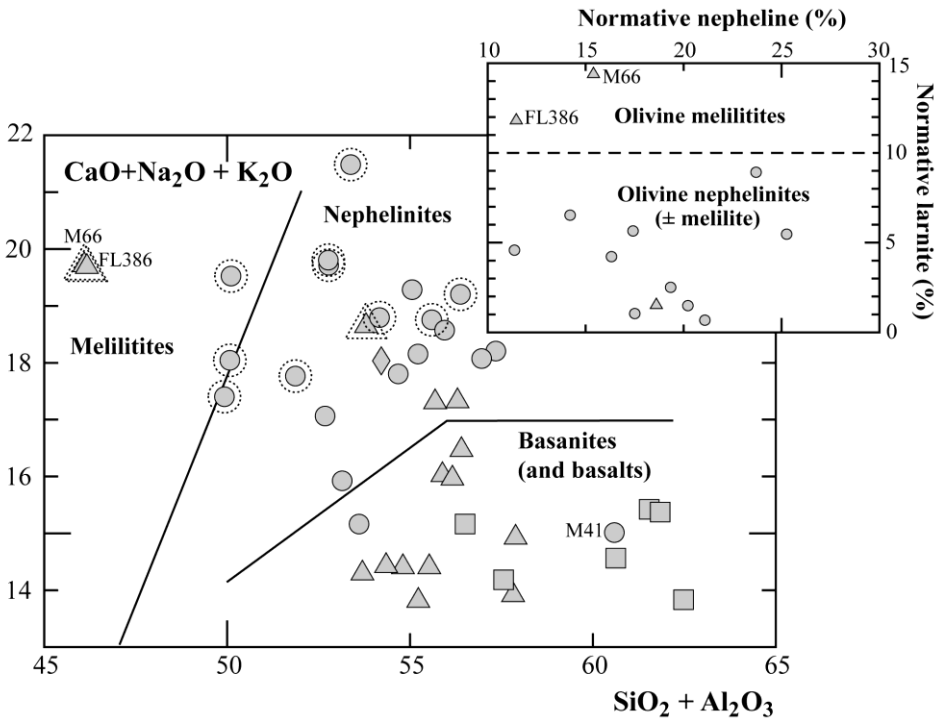
Normative nepheline (%)
10
15
20
25
30
15
10
5
0
Normative larnite (%)
M66
FL386
Olivine melilitites
Olivine nephelinites
(± melilite)
22
20
18
16
14
CaO+Na2O + K2O
Nephelinites
M66
FL386
Melilitites
Basanites
(and basalts)
M41
45
50
55
60
65
SiO2 + Al2O3

860

861 Fig. 5

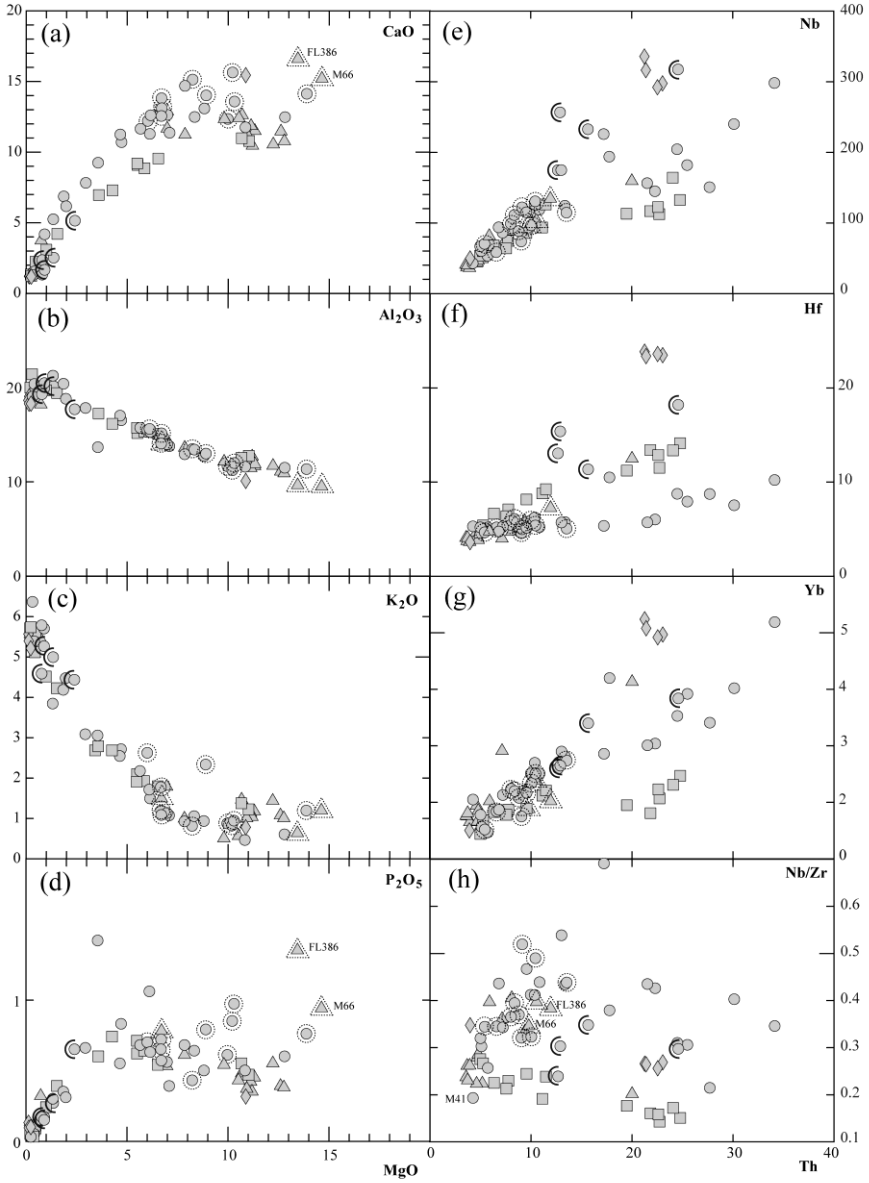
(a)
CaO
FL386
M66
(e)
Nb
(b)
Al_2O_3
(f)
Hf
(c)
K_2O
(g)
Yb
(d)
P_2O_5
(h)
Nb/Zr
FL386
M66
FL386
M66
M41
MgO
Th

862

863 Fig. 6

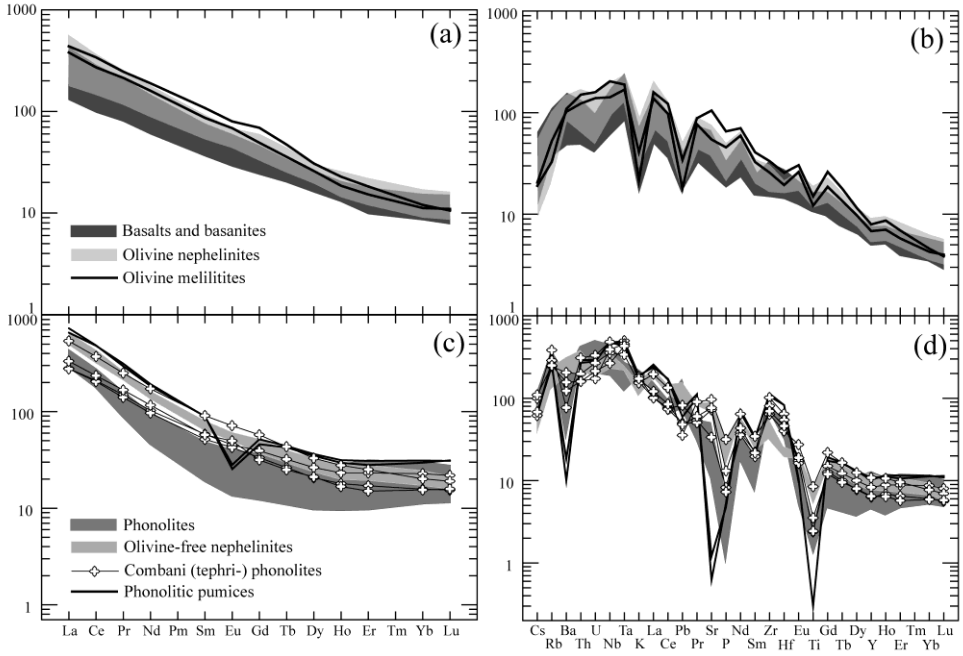

864

865

866 Fig. 7

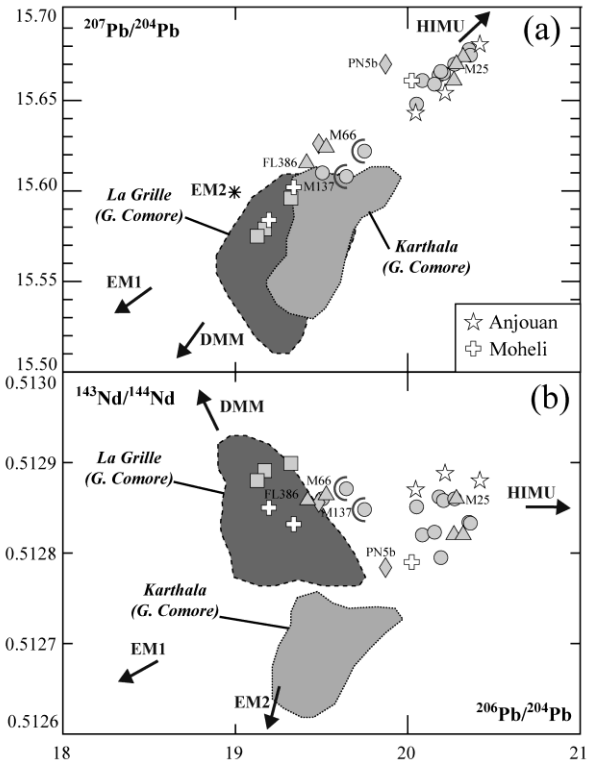

867

868 Fig. 8

869

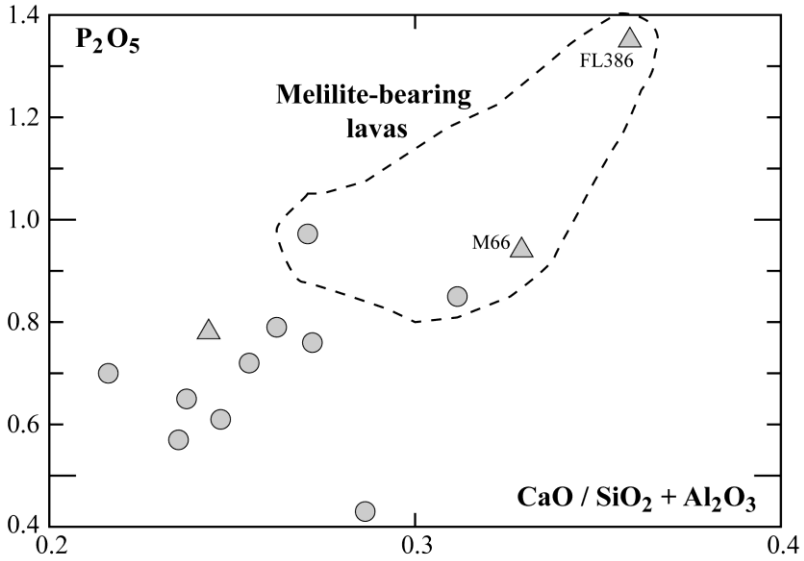
1.4
1.2
1.0
0.8
0.6
0.4
0.2
0.3
0.4
P2O5
CaO / SiO2 + Al2O3
Melilite-bearing
lavas
FL386
M66

870

871 Fig. 9

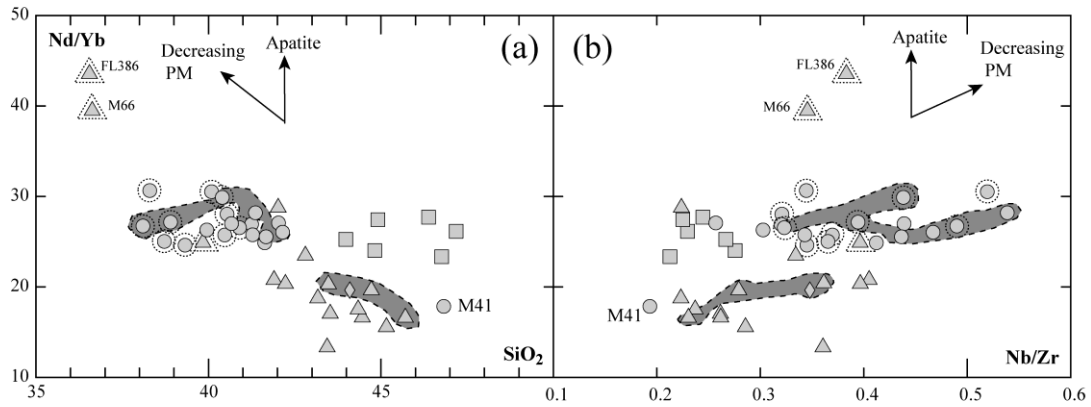

872

873 Fig. 10

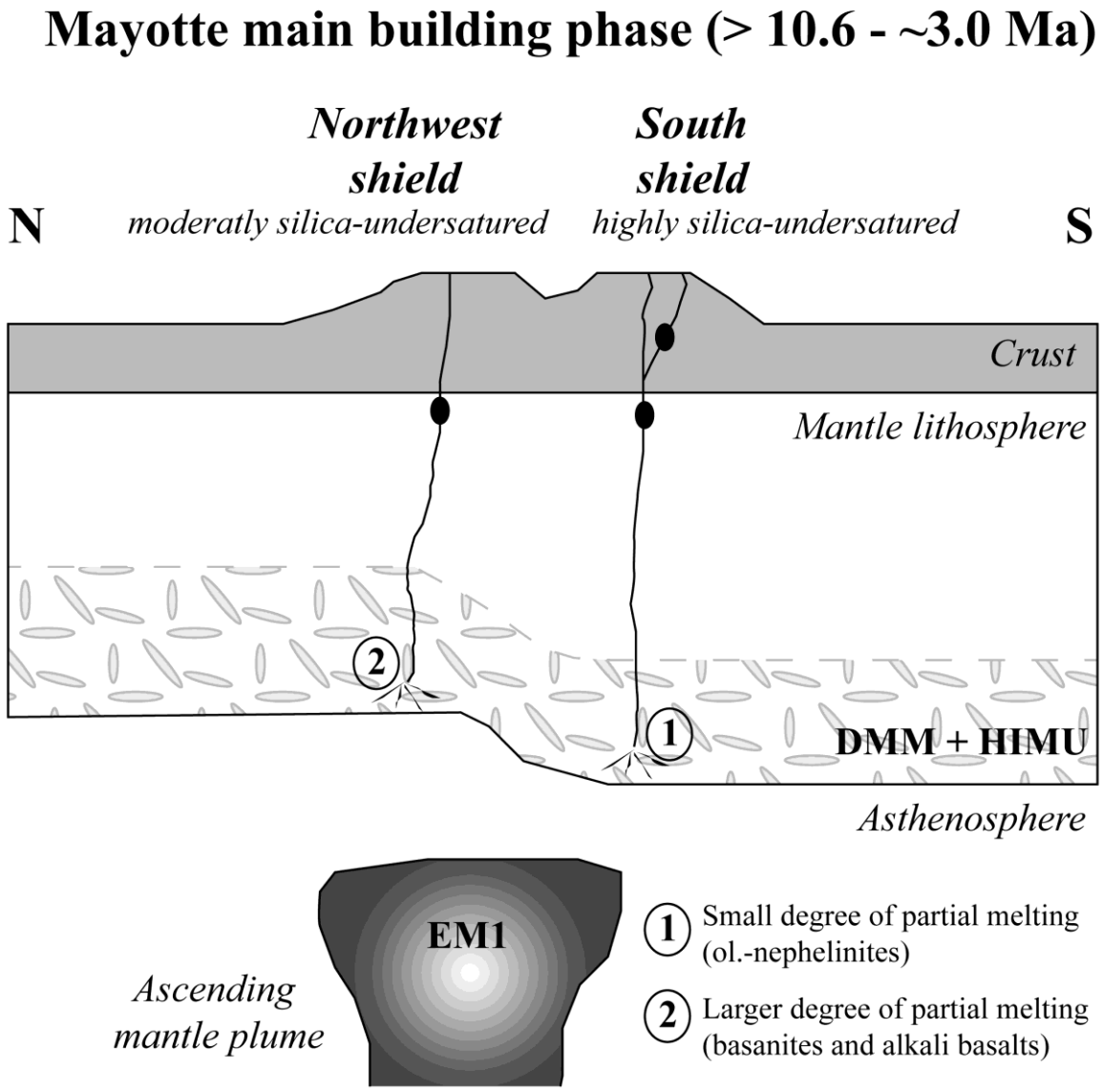

874

875 Fig. 11

Table 1. Dating results from ^{40}Ar–^{39}Ar geochronology for Mayotte samples

Sample				Plateau age			Inverse isochron age					Integrated age	Preferred age	Remark
Unit	**Number**	**Location**	**Petrological type**	**Type**	**Age (Ma)**	**Steps**	**Type**	**Age (Ma)**	**$^{40}Ar/^{36}Ar_i$**	**MSWD**	**Steps**	**Age (Ma)**	**Age (Ma)**	
Northwest	M104	Lava flow	Basanite	SMA	6.1 ± 0.3	1-3		4.3 ± 0.1	311 ± 10	0,1	1-6	5.0 ± 0.1	6.1 ± 0.3	SMA is maximum age Data too clustered on isochron
	M112	Dyke	Ol.-nephelinite	SMA	5.2 ± 0.3	1-3		4.4 ± 1.0	305 ± 10	2,4	1-5	5.3 ± 0.1	4.4 ± 1.0	
	M108	Dyke in M104	Basanite	SMA	3.8 ± 0.1	1-4		4.2 ± 0.8	291 ± 10	7,1	1-6, 8	3.2 ± 0.1	3.8 ± 0.1	
	M25	Lava flow	Alkali basalt	NO	-	-		2.0 ± 0.9	382 ± 46	26,8	1-4	3.2 ± 0.1	2.0 ± 0.9	Maximum age
	M20	Dyke	Basanite	SMA	0.6 ± 1.25	4-5	NO	-	-	-	-	8.9 ± 0.2	< 1 Ma	Maximum age
	M59	Lava flow	Basanite	WMP	0.8 ± 0.2	1-5		0.8 ± 0.1	303 ± 150	0,1	1-6	0.8 ± 0.2	0.8 ± 0.2	Data too clustered on isochron
North central	M97	Lava flow	Basanite	SMA	1.9 ± 0.1	1-5		2.4 ± 0.3	291 ± 6	4,8	1-5	1.8 ± 0.1	2.4 ± 0.3	
	M4	Lava flow	Tephrite	NO	-	-		2.3 ± 0.3	240 ± 30	12,7	1-3, 5-7	3.5 ± 0.6	2.3 ± 0.3	Maximum age
	M29	Dome	Trachyte	NO	-	-	NO	-	-	-	-	2.9 ± 0.6	< 3 Ma	Maximum age
	M123	Lava flow	Tephriphonolite		1.2 ± 0.1 / 1.4 ± 0.1	-	NO	-	-	-	-	1.2 ± 0.1 / 1.4 ± 0.1	1.4 ± 0.1	
	M56	Lava flow	Basaltic trachy-andesite	SMA	1.5 ± 0.6	1-3		1.4 ± 0.1	311 ± 11	2,6	1-4	1.4 ± 0.1	1.4 ± 0.1	
	M82	Lava flow	Basanite	SMA	1.4 ± 0.1	1-4		2.1 ± 0.1	265 ± 10	0,9	1-4	1.1 ± 0.1	1.1 ± 0.1	
	M58	Lava flow	Phonolite	SMA	0.2 ± 0.1	1-3		0.8 ± 0.1	345 ± 18	4,3	1-6	0.6 ± 0.1	0.8 ± 0.1	Nice isochron
Petite Terre	M53	Strombolian cone	Alkali basalt	NO	-	-	NO	-	-	-	-	0.5 ±0.1	0.2 ± 0.1	All individual steps below 0.2 Ma
South	M137	Lava flow	Ol.-nephelinite	NO	-	-		5.0 ± 0.3	319 ± 2	1,1	1-6	13.1 ± 0.2	5.0 ± 0.3	
	M41	Lava flow	Alkali basalt	NO	-	-		10.6 ± 0.5	270 ± 20	5,9	2-6	6.2 ± 0.1	10.6 ± 0.5	Steps used are the richest in ^{39}Ar
	M140	Lava flow	Ol.-free neph.	WMP	5.9 ± 0.1	1-4		6.1 ± 0.1	306 ± 5	2,2	1-5	5.8 ± 0.1	5.9 ± 0.1	
	M93	Lava flow	Ol.-nephelinite	NO	-	-		3.4 ± 0.2	308 ± 6	4,8	1-4	4.4 ± 0.1	3.4 ± 0.2	
	M132	Lava flow	Ol.- nephelinite	SMA	3.8 ± 0.1	2-4		4.0 ± 0.3	302 ± 7	5,5	1-6	4.7 ± 0.1	4.0 ± 0.3	
	M38	Lava flow	Ol.-nephelinite	SMA	4.6 ± 0.1	1-2	NO	-	-	-	-	3.9 ± 0.1	3.9 ± 0.1	The integrated age is preferred to badly defined plateau
	M39A	Dome	Phonolite	WMP	3.9 ± 0.4	2-7		4.7 ± 0.9	263 ± 49	0,8	2-7	4.3 ± 0.1	3.9 ± 0.4	Good plateau
	M55	Lava flow	Ol.-free neph.	NO	-	-		3.6 ± 0.4	291 ± 42	5,9	1-4, 7	3.8 ± 0.5	3.6 ± 0.4	
	M115	Lava flow	Ol.-nephelinite	NO	-	-		1.9 ± 0.2	327 ± 11	6,4	1-7	2.1 ± 0.4	1.9 ± 0.2	
	M95	Lava flow	Ol.-nephelinite	SMA	2.5 ± 0.2	1-2	NO	-	-	-	-	1.5 ± 0.8	< 2.5 Ma	

For each sample, the plateau age and the isochron age are given when available; the preferred age is indicated in the last column.
MSWD: mean square weighted deviation. SMA: simple mean age, WMP: weighed plateau age.
Type of statistical approach: NO: no plateau or isochron could be calculated; SMA: simple mean age; WMP: weighed mean plateau age

Table 2. Major and trace elements data for Mayotte

	Phonolitic pumices			Alkali basalts			Basanites							Olivine melilitites	
Sample	M54[1]	PN5a[2]	PN15[2]	M25[1]	M41[1]	M75[1]	M35[1]	M60[1]	M82[1]	M97[1]	M108[1]	PN3[2]	PN5b[2]	FL386[2]	M66[1]
Location	PT	PT	PT	NW	S	NC	S	NW	NC	NC	NW	S	PT	NW	NW
Major elements (wt. %)															
SiO_2	58.42	57.80	57.70	45.71	46.82	47.18	42.03	42.02	44.91	43.98	44.72	41.67	44.08	36.55	36.63
TiO_2	-	0.07	0.06	2.28	2.75	2.74	3.45	3.14	3.28	2.77	2.26	2.36	1.91	3.01	2.44
Al_2O_3	19.21	18.30	18.30	12.20	13.79	15.32	11.60	11.70	15.74	12.55	11.46	11.50	10.11	9.64	9.49
$Fe_2O_{3\ (total)}$	5.82	5.80	5.80	13.52	12.80	12.81	13.86	14.03	12.57	13.84	13.03	12.42	10.42	14.29	13.25
MnO	0.25	0.24	0.25	0.18	0.16	0.17	0.16	0.17	0.18	0.20	0.19	0.22	0.15	0.23	0.21
MgO	0.13	0.14	0.24	10.93	7.09	5.85	10.84	12.22	5.49	10.66	11.12	12.80	10.86	13.44	14.63
CaO	1.20	1.21	1.17	11.24	11.35	8.84	11.74	10.53	9.18	10.97	11.83	12.46	15.46	16.57	15.18
Na_2O	8.24	7.80	7.99	2.70	2.61	3.09	2.98	2.35	3.50	2.84	3.02	2.88	1.78	2.50	3.36
K_2O	5.55	5.38	5.20	0.99	1.06	1.91	0.45	1.42	1.89	1.36	1.12	0.59	0.79	0.62	1.18
P_2O_5	0.13	0.09	0.10	0.37	0.39	0.64	0.50	0.55	0.71	0.55	0.42	0.60	0.32	1.35	0.94
LOI	0.93	2.54	3.29	-0.15	1.10	1.45	2.39	1.08	2.54	0.18	0.73	3.40	3.78	2.95	1.63
Total	99.88	99.31	100.10	99.97	99.92	100.00	100.00	99.21	99.99	99.90	99.90	100.88	98.38	101.15	98.94
$_N$Larnite	-	-	-	-	-	-	-	-	-	-	-	-	-	11.80	14.38
$_N$Nepheline	-	-	-	5.13	0.31	0.59	8.93	8.02	5.76	8.42	9.61	12.13	6.87	11.46	15.40
Trace elements (ppm)															
Li	-	23.7	24.5	-	-	-	-	-	-	-	-	7.6	9.6	11.4	-
Be	5.9	5.8	5.6	1.5	-	-	2.0	-	2.1	-	-	1.8	1.2	2.4	1.7
Rb	162	163	149	22	23	43	62	38	50	33	30	20	21	20	32
Sr	26.1	32.6	25.0	530	495	913	761	609	980	948	494	828	419	2087	1083
Ba	114	136	121	316	327	707	563	546	652	546	407	648	238	719	674
Cs	1.28	1.55	1.41	0.25	-	0.44	0.58	0.52	0.51	0.27	0.26	0.54	0.36	0.40	0.43
V	-	-	-	265	290	205	322	242	219	253	258	279	258	255	246
Cr	-	-	-	787	149	145	563	380	58	402	714	626	472	465	626
Ni	-	-	-	263	116	119	277	364	48	265	238	357	168	270	365
Co	-	-	-	62	49	40	65	71	35	62	59	66	45	64	65
Sc	-	13	12	-	-	-	-	-	-	-	-	28	51	25	-
Cu	-	10	6.5	89	114	45	81	62	40	70	100	75	74	73	67
Zn	207	185	162	132	126	159	124	140	141	138	111	109	74	137	124
Y	46	46	44	24	25	28	22	22	27	24	21	27	21	34	29
Zr	1141	1262	1195	173	222	325	208	218	303	225	156	215	145	350	270
Nb	292	336	316	40	43	75	53	49	68	59	44	94	50	134	93
Hf	24	24	23	4.1	5.3	7.1	5.2	5.2	6.7	5.4	4.2	4.8	3.5	7.3	5.5
Ta	18	17	16	3.0	3.0	5.0	4.0	4.0	5.0	4.0	3.5	5.0	2.5	7.0	6.0
La	151.2	171.3	166.2	30.9	37.5	55.6	42.7	43.2	50.3	45.8	36.1	58.9	35.6	102.9	89.5
Ce	282.6	291.0	281.9	64.9	76.7	112.8	85.9	91.3	108.5	90.9	74.5	113.9	66.5	204.6	163.2
Pr	28.7	26.8	25.6	7.20	8.85	12.9	10.1	10.4	12.9	10.5	8.50	12.6	7.43	22.4	19.5
Nd	88.2	85.5	83.6	30.0	36.6	48.9	39.8	41.7	50.2	42.4	32.6	47.8	29.6	88.0	74.2
Sm	13.5	13.6	13.2	6.46	7.56	9.59	8.41	8.35	9.66	7.81	6.46	9.14	5.66	16.5	13.3
Eu	1.63	1.65	1.60	2.09	2.45	3.12	2.62	2.67	3.11	2.64	2.15	2.73	1.81	4.68	4.02
Gd	9.55	10.5	10.5	6.05	6.80	8.05	7.00	7.15	8.10	6.90	5.90	8.55	5.40	14.0	10.0
Tb	1.60	1.65	1.65	0.80	0.90	1.05	0.90	0.95	1.15	0.95	0.80	1.15	0.75	1.75	1.35
Dy	8.91	9.24	8.84	4.60	5.00	5.79	4.68	5.06	5.90	5.15	4.45	5.69	4.07	7.81	6.60
Ho	1.66	1.78	1.75	0.79	0.86	0.97	0.78	0.81	0.99	0.87	0.76	1.02	0.75	1.29	1.05
Er	4.73	5.13	5.04	2.04	2.24	2.53	1.80	1.97	2.37	2.15	1.99	2.56	1.87	3.03	2.53
Yb	4.92	5.24	5.08	1.81	2.05	1.87	1.47	1.45	1.83	1.68	1.66	1.87	1.51	2.02	1.88
Lu	0.79	0.76	0.75	0.26	0.28	0.28	0.19	0.21	0.27	0.21	0.24	0.25	0.21	0.26	0.27
Th	22.6	21.3	21.4	3.7	4.3	7.8	5.7	5.2	6.4	5.3	4.7	6.8	3.9	12.0	9.8
U	5.8	5.8	5.7	0.9	1.0	1.8	1.3	1.4	1.7	1.4	1.0	1.5	0.8	3.2	2.8
Pb	11.3	19.3	8.9	2.9	2.8	4.6	3.1	2.6	3.8	2.9	3.5	4.7	5.2	5.1	2.7

	Olivine nephelinites														
Sample	FL468[2]	J2[2]	M19[1]	M50[1]	M88[1]	M89[1]	M112[1]	M129[1]	M132[1]	M133[1]	M135[1]	M137[1]	M138[1]	PN2[2]	PN12f[2]
Location	S	S	NW	S	S	S	NW	S	S	S	S	S	S	S	S
Major elements (wt. %)															
SiO_2	41.36	42.15	39.84	40.09	39.32	40.47	43.44	38.30	40.90	40.40	41.28	40.54	38.72	38.90	38.10
TiO_2	2.31	2.52	3.07	2.65	3.41	3.26	2.17	3.51	2.83	2.36	2.98	2.41	2.84	3.10	2.56
Al_2O_3	15.62	12.93	13.98	14.10	13.48	15.15	12.27	11.65	15.50	13.00	13.42	11.35	14.07	11.23	12.00
$Fe_2O_{3\ (total)}$	12.98	12.45	14.43	12.81	12.58	12.77	12.91	12.86	12.06	11.74	12.52	12.20	12.56	13.67	12.70
MnO	0.28	0.23	0.23	0.23	0.16	0.19	0.20	0.18	0.21	0.24	0.20	0.21	0.23	0.22	0.24
MgO	6.11	7.85	6.71	6.69	8.23	6.70	10.68	9.97	6.01	8.90	8.33	13.88	6.68	10.21	10.30
CaO	11.27	14.67	13.11	13.80	15.12	13.09	12.60	12.33	12.19	14.00	12.47	14.11	12.54	15.62	13.56
Na_2O	5.11	3.71	4.06	3.82	3.80	4.60	3.26	4.22	4.41	5.17	4.30	2.48	5.51	3.10	3.56
K_2O	1.70	0.91	1.48	1.18	0.80	1.07	1.45	0.86	2.61	2.32	1.04	1.18	1.76	0.81	0.93
P_2O_5	1.06	0.68	0.78	0.72	0.43	0.57	0.48	0.61	0.70	0.79	0.64	0.76	0.65	0.85	0.97
LOI	2.73	2.84	2.20	3.93	2.63	2.13	0.66	4.02	2.63	0.72	2.45	0.59	3.49	2.59	4.55
Total	100.54	100.93	99.89	100.02	99.96	100.00	100.12	98.51	100.05	99.64	99.63	99.62	99.05	100.31	99.47
$_N$Larnite	-	-	1.52	1.03	5.65	0.68	-	2.37	1.49	8.92	-	4.58	5.47	6.53	4.22
$_N$Nepheline	23.42	17.01	18.61	17.51	17.42	21.09	14.94	19.34	20.22	23.70	19.71	11.37	25.26	14.21	16.32
Trace elements (ppm)															
Li	13.3	10.5	-	-	-	-	-	-	-	-	-	-	-	10.3	16.0
Be	3.5	2.8	3.0	2.6	1.5	2.0	-	-	2.8	2.1	2.1	-	2.6	2.3	2.6
Rb	45	30	42	22	11	14	45	28	58	65	17	28	48	27	27
Sr	1528	878	843	1064	727	873	645	757	1143	1297	815	746	1072	1154	1368
Ba	946	858	920	875	587	829	568	587	849	1069	721	572	867	743	960
Cs	0.80	2.65	1.05	0.65	0.36	0.54	0.62	0.36	0.68	0.65	0.78	0.24	1.20	0.55	0.20
V	252	320	324	307	372	305	274	304	241	221	311	212	306	330	286
Cr	62	183	76	110	180	77	581	451	109	315	507	547	182	337	332
Ni	46	98	53	55	69	41	200	193	61	143	160	300	86	181	165
Co	43	59	48	42	46	39	57	54	36	41	50	78	46	60	54
Sc	16	32	-	-	-	-	-	-	-	-	-	-	-	30	23
Cu	65	150	73	83	88	37	105	83	55	67	94	65	85	102	77
Zn	145	118	143	124	96	113	117	107	135	116	128	118	135	123	124
Y	40	31	31	29	24	27	24	23	31	37	29	24	29	32	33
Zr	324	246	262	235	170	239	185	205	299	261	251	230	271	282	266
Nb	175	115	104	122	59	89	67	70	97	115	86	74	99	111	131
Hf	5.7	5.1	5.7	5.0	5.2	5.6	4.0	4.7	5.9	5.1	5.3	4.6	5.5	6.1	5.4
Ta	9.0	5.0	7.0	6.5	4.5	6.5	4.5	5.0	7.5	7.5	6.5	5.0	6.5	5.5	7.0
La	118.8	76.0	83.6	91.2	47.7	65.0	53.9	50.1	78.0	134.7	65.1	84.2	73.9	74.3	92.0
Ce	221.6	140.6	151.9	168.0	99.6	129.1	98.2	99.4	145.7	218.9	125.4	120.1	136.0	140.0	168.3
Pr	23.0	15.1	16.4	17.6	11.2	14.1	10.4	11.8	16.1	23.5	14.2	13.1	14.9	15.5	17.9
Nd	81.8	56.5	59.2	65.6	45.3	53.5	38.8	46.6	62.1	81.9	54.9	49.1	56.0	59.7	67.1
Sm	14.1	10.3	10.2	10.9	8.23	9.49	7.11	8.83	10.9	13.1	10.0	8.50	9.93	11.5	11.9
Eu	3.98	3.01	3.18	3.31	2.55	2.92	2.21	2.71	3.38	3.89	3.12	2.67	3.06	3.38	3.49
Gd	12.5	9.50	8.75	8.90	7.10	7.75	6.00	7.15	8.90	10.0	8.25	7.05	8.20	10.5	10.5
Tb	1.65	1.25	1.20	1.20	0.95	1.05	0.85	0.95	1.25	1.40	1.15	0.95	1.15	1.35	1.40
Dy	7.74	6.13	6.38	6.05	5.00	5.68	4.65	4.96	6.40	7.35	6.04	5.08	6.08	6.79	7.05
Ho	1.44	1.13	1.12	1.04	0.90	0.99	0.82	0.83	1.16	1.28	1.02	0.81	1.06	1.20	1.28
Er	3.65	2.86	2.96	2.70	2.27	2.55	2.06	1.98	2.88	3.36	2.59	2.16	2.65	2.97	3.25
Yb	2.90	2.17	2.38	2.15	1.84	2.08	1.91	1.52	2.34	2.74	2.13	1.75	2.24	2.20	2.51
Lu	0.40	0.29	0.35	0.31	0.27	0.31	0.27	0.21	0.33	0.39	0.30	0.25	0.33	0.29	0.34
Th	13.0	9.6	10.6	9.1	6.6	8.8	7.1	5.4	10.0	13.5	7.2	9.1	8.0	8.4	10.4
U	5.1	2.2	2.3	2.2	1.6	2.0	1.6	1.3	2.6	3.2	1.5	2.0	1.9	2.1	3.1
Pb	7.4	5.8	6.0	5.3	3.3	4.2	4.7	7.6	6.2	7.9	4.3	4.7	11.0	5.0	6.4

	Olivine-free nephelinites		Tephrites		Tephri-phonolites				Phonolites						
Sample	M140[1]	PN8[2]	J7[2]	M4[1]	FL478[2]	M91[1]	M123[1]	M127[1]	FL426[2]	FL442[2]	M58[1]	M103[1]	M131[1]	PN7[2]	PN11[2]
Location	S	S	NC	NC	S[C]	S	NC	NW	S[C]	S[C]	NC	S[C]	S	S	NC
Major elements (wt. %)															
SiO_2	47.15	46.02	49.02	46.38	49.94	50.24	55.00	51.66	53.55	54.58	58.98	54.34	54.47	53.91	55.85
TiO_2	1.09	1.26	2.46	2.94	1.70	0.67	1.22	1.03	0.48	0.49	0.33	0.71	0.25	0.31	0.30
Al_2O_3	20.41	18.82	16.16	15.18	17.70	19.96	19.43	18.22	19.31	20.48	20.00	20.16	20.39	19.07	21.42
$Fe_2O_{3\,(total)}$	7.89	7.88	10.91	12.42	9.42	6.54	6.21	8.31	5.80	4.78	3.49	5.62	4.37	5.67	2.75
MnO	0.22	0.29	0.18	0.17	0.25	0.27	0.14	0.28	0.27	0.19	0.14	0.19	0.22	0.29	0.17
MgO	1.85	1.97	4.26	5.50	2.40	0.90	1.53	0.73	0.78	0.90	0.21	1.35	0.41	0.33	0.24
CaO	6.85	6.15	7.28	9.08	5.13	4.17	4.19	3.73	2.34	1.65	1.32	2.51	1.54	1.29	1.30
Na_2O	6.79	8.25	4.82	4.27	7.38	7.25	6.60	8.07	8.24	9.37	8.03	8.95	8.77	8.29	9.61
K_2O	4.17	4.46	2.67	2.08	4.42	5.69	4.21	5.43	4.57	5.25	5.70	4.98	5.37	6.35	5.72
P_2O_5	0.35	0.31	0.74	0.62	0.65	0.17	0.39	0.32	0.17	0.15	0.05	0.27	0.05	0.02	0.03
LOI	3.32	4.13	0.59	1.35	1.26	4.25	1.11	2.61	3.12	1.22	1.65	1.02	4.09	3.78	1.32
Total	100.09	99.15	99.09	98.64	100.25	100.11	100.03	100.39	98.63	99.07	99.90	100.10	99.93	98.75	98.71
$_N$Larnite	-	-	-	-	-	-	-	-	-	-	-	-	-	-	-
$_N$Nepheline	-	-	-	-	-	-	-	-	-	-	-	-	-	-	-
Trace elements (ppm)															
Li	-	21.5	14.0	-	13.4	-	-	-	7.1	14.4	-	-	-	2.6	17.6
Be	4.5	7.3	3.5	2.5	3.3	7.5	3.4	4.3	6.7	4.2	8.2	2.1	8.7	10.7	6.9
Rb	131	146	78.1	30.7	146	214	104	174	230	172	187	150	162	242	202
Sr	1341	1828	1091	964	1916	1284	1040	1428	668	1439	213	1520	764	1035	268
Ba	1262	2064	856	788	1350	1380	1084	1765	506	811	561	1032	277	764	206
Cs	1.28	1.21	1.08	1.24	1.29	1.95	1.34	0.83	2.09	1.43	1.90	2.30	2.13	1.32	2.58
V	64	107	177	224	103	53	54	15.7	10.8	11	2.8	31	9.2	9.1	15
Cr	-	3.5	59	153	12	-	-	-	1.2	11	-	19	-	-	0.4
Ni	-	3.0	55	90	15	-	5.5	-	1.7	12	-	18	-	-	0.5
Co	12	12	35	44	16	5.5	10	5.2	2.3	3.2	1.2	5.8	1.0	1.4	1.4
Sc	-	2.0	14	-	5.4	-	-	-	1.6	1.4	-	-	-	0.9	1.1
Cu	16	12	41	53	15	4.8	11	-	0.7	1.9	-	5.9	-	0.5	1.2
Zn	156	179	154	155	146	194	135	172	189	132	144	128	175	246	137
Y	33	53	31	27	47	38	25	41	36	27	24	28	32	55	19
Zr	340	596	529	350	668	594	640	790	1067	846	879	731	701	862	953
Nb	145	240	126	86	233	182	113	159	317	257	132	175	151	298	164
Hf	6.0	7.5	9.3	8.2	11.4	7.9	11.2	12.5	18.2	15.4	14.1	13.1	8.7	10.2	13.4
Ta	9.0	8.0	6.0	6.0	13	5.0	9.5	14	18	17	10	16	6.0	5.0	4.5
La	116.1	154.4	74.4	65.2	127.0	97.2	79.3	113.7	66.0	65.3	98.7	78.4	85.8	102.9	81.7
Ce	191.6	243.2	138.2	125.8	224.1	142.8	145.4	203.0	126.6	123.1	138.3	141.9	140.8	168.4	106.0
Pr	19.5	22.1	15.0	13.8	22.9	14.6	15.2	23.3	13.6	12.8	12.0	15.3	12.5	14.8	7.99
Nd	64.4	73.2	55.6	52.4	80.2	45.8	48.2	83.5	47.9	44.9	35.3	54.3	38.7	45.2	21.2
Sm	9.94	11.9	10.5	9.72	14.0	7.37	7.16	13.8	8.98	7.93	4.83	8.81	6.14	7.60	2.83
Eu	3.16	3.53	3.19	3.14	4.21	2.33	2.51	4.13	2.66	2.50	1.22	2.92	1.91	2.41	0.78
Gd	7.80	10.5	9.40	3.75	12.0	6.40	5.95	10.0	8.15	6.90	3.35	6.50	4.80	7.65	2.45
Tb	1.15	1.50	1.30	1.05	1.65	1.00	0.85	1.50	1.20	1.00	0.55	0.95	0.80	1.30	0.40
Dy	6.48	8.35	6.28	5.90	8.41	6.23	4.59	8.43	6.74	5.25	3.65	5.37	5.60	7.78	2.44
Ho	1.17	1.64	1.14	0.89	1.58	1.23	0.82	1.42	1.32	1.02	0.71	0.85	1.06	1.64	0.56
Er	3.22	4.67	2.79	2.39	4.19	3.72	2.31	3.96	3.86	2.84	1.97	2.50	3.21	5.25	1.87
Yb	3.04	4.02	2.21	1.89	3.40	3.92	1.95	4.13	3.84	2.65	2.47	2.60	3.41	5.19	2.31
Lu	0.45	0.53	0.29	0.29	0.47	0.57	0.31	0.60	0.54	0.38	0.35	0.39	0.50	0.71	0.34
Th	22.3	30.1	11.5	9.6	15.7	25.5	19.5	20.0	24.6	12.9	24.8	12.7	27.7	34.1	24.1
U	5.0	5.1	3.2	2.6	5.4	7.6	4.9	4.6	6.7	3.5	3.9	4.3	7.4	10.3	8.4
Pb	12.7	23.4	5.9	5.0	5.3	20.8	9.6	11.4	12.3	7.5	16.2	7.2	17.9	26.3	11.2

S: south domain; S^C: Combani; NW: northwest domain; NC: north central domain; PT: Petite Terre. $_N$Larnite for normative larnite ; $_N$Nepheline for normative nepheline. CIPW norms was calculated for basic lavas using the ratio: $Fe_2O_3/Fe_2O_{3(total)}$=0.15. (1) Samples collected in 2001, major and trace elements analyzed by ICP-AES and ICP-MS respectively (CRPG, Nancy, France). (2) Samples collected during two field trips in 2010 and 2011, major elements analyzed by ICP-AES (PSO/IUEM, Brest, France) following the analytical method described by Cotten et al (1995), trace elements analyzed by ICP-MS (PSO/IUEM, Brest, France) following the sample preparation and analysis method of Barrat et al (1996).

Table 3. Sr, Nd, Pb isotopic data for Mayotte.

(1) S: south domain; S^C: Combani Massif; NW: northwest domain; NC: north central domain; PT: Petite Terre domain (see Fig. 2c for domain location).

(2) Sr and Nd isotopic ratios measured in 2003 on a TI-MS (Laboratoire Magmas et Volcans, Clermont-Ferrand, France) – Debeuf (2004). Average value of NBS 987 (standard for Sr) is $^{87}Sr/^{86}Sr = 0.710253 \pm 0.000020$ (1σ ; n=39) and average value of Rennes-AMES (internal standard for Nd) is $^{143}Nd/^{144}Nd = 0.511960 \pm 0.000010$ (1σ ; n=41).

(3) Sr and Nd isotopic ratios measured in 2013 on a TI-MS (PSO/IUEM, Brest, France). Sr and Nd isotopic values are corrected for mass fractionation to $^{88}Sr/^{86}Sr = 8.372509$ and $^{146}Nd/^{144}Nd = 0.721903$ respectively. Average value of NBS 987 is $^{87}Sr/^{86}Sr = 0.710237 \pm 0.000006$ (2σ ; n=8) and average value of La Jolla (standard for Nd) is $^{143}Nd/^{144}Nd = 0.511873 \pm 0.000008$ (2σ ; n=6). Pb isotopic ratios measurements were performed by a MC-ICP-MS (PSO/IFREMER, Brest, France). Pb isotopic values are corrected for drift of $^{205}Tl/^{203}Tl$ ratio and for the blank. Average values of NIST SRM 981 (standard for Pb) are $^{206}Pb/^{204}Pb = 16.9314 \pm 0.0005$ (2σ ; n=7); $^{207}Pb/^{204}Pb = 15.4850 \pm 0.0006$ (2σ ; n=7); $^{208}Pb/^{204}Pb = 36.6764 \pm 0.0018$ (2σ ; n=7).

(4) Nd and Pb isotopic ratios measured in february 2014 on a MC-ICP-MS (PSO/IFREMER, Brest, France). Nd isotopic values are corrected for mass fractionation to $^{146}Nd/^{144}Nd = 0.721903$. Average values of JNDi and La Jolla (standards for Nd) are $^{143}Nd/^{144}Nd = 0.512105 \pm 0.000008$ (2σ ; n=6) and $^{143}Nd/^{144}Nd = 0.511859 \pm 0.000010$ (2σ ; n=4) respectively. Pb isotopic values are corrected for drift of $^{205}Tl/^{203}Tl$ ratio and for the blank. Average values of NIST SRM 981 (standard for Pb) are $^{206}Pb/^{204}Pb = 16.9300 \pm 0.0006$ (2σ ; n=10); $^{207}Pb/^{204}Pb = 15.4844 \pm 0.0007$ (2σ ; n=10); $^{208}Pb/^{204}Pb = 36.6743 \pm 0.0019$ (2σ ; n=10).

Sample	Rock Type	Location[1]	$^{87}Sr/^{86}Sr$	2σ	$^{143}Nd/^{144}Nd$	2σ	$^{206}Pb/^{204}Pb$	2σ	$^{207}Pb/^{204}Pb$	2σ	$^{208}Pb/^{204}Pb$	2σ
PN5a	Phon. pumice	PT	-	-	0.512856[4]	0.000008	19.4841[4]	0.0006	15.6263[4]	0.0006	39.377[4]	0.002
M25	Alkali basalt	NW	0.703350[2]	0.000006	0.512860[4]	0.000004	20.2819[4]	0.0006	15.6699[4]	0.0007	39.965[4]	0.002
M41	Alkali basalt	S	0.703830[2]	0.000006	0.512720[2]	0.000004	-	-	-	-	-	-
M60	Basanite	NW	0.703300[2]	0.000006	0.512860[2]	0.000004	-	-	-	-	-	-
M82	Basanite	NC	-	-	0.512860[2]	0.000004	-	-	-	-	-	-
M97	Basanite	NC	0.703350[2]	0.000006	0.512880[2]	0.000004	19.1269[4]	0.0006	15.5746[4]	0.0006	39.059[4]	0.002
M108	Basanite	NW	0.703390[2]	0.000006	0.512820[2]	0.000004	20.3206[4]	0.0008	15.6738[4]	0.0007	40.028[4]	0.002
PN3	Basanite	S	0.703241[3]	0.000006	0.512862[3]	0.000010	20.1820[3]	0.0010	15.6641[3]	0.0009	39.929[3]	0.003
PN5b	Basanite	PT	-	-	0.512784[4]	0.000004	19.8709[4]	0.0009	15.6698[4]	0.0008	39.718[4]	0.003
FL386	Ol.-melilitite	NW	0.703254[3]	0.000006	0.512860[3]	0.000008	19.4139[3]	0.0007	15.6150[3]	0.0007	39.282[3]	0.002
M66	Ol.-melilitite	NW	-	-	0.512864[4]	0.000003	19.5269[4]	0.0006	15.6238[4]	0.0006	39.379[4]	0.002
FL468	Ol.-nephelinite	S	0.703307[3]	0.000006	0.512823[3]	0.000004	20.1553[3]	0.0008	15.6589[3]	0.0007	39.883[3]	0.002
J2	Ol.-nephelinite	S	0.703418[3]	0.000008	0.512795[3]	0.000006	20.1919[3]	0.0006	15.6664[3]	0.0006	39.930[3]	0.002
M112	Ol.-nephelinite	NW	0.703380[2]	0.000006	0.512820[2]	0.000004	20.2677[4]	0.0006	15.6606[4]	0.0008	39.961[4]	0.003
M132	Ol.-nephelinite	S	0.703410[2]	0.000006	0.512860[2]	0.000004	20.2718[4]	0.0007	15.6700[4]	0.0006	39.993[4]	0.002
M133	Ol.-nephelinite	S	-	-	0.512820[4]	0.000004	20.0849[4]	0.0005	15.6608[4]	0.0005	39.856[4]	0.001
M137	Ol.-nephelinite	S	0.703320[2]	0.000006	0.512860[2]	0.000004	19.5055[4]	0.0005	15.6096[4]	0.0006	39.391[4]	0.002
PN2	Ol.-nephelinite	S	0.703253[3]	0.000006	0.512851[3]	0.000004	20.0507[3]	0.0009	15.6482[3]	0.0009	39.799[3]	0.003
PN12f	Ol.-nephelinite	S	-	-	0.512833[4]	0.000004	20.3627[4]	0.0007	15.6746[4]	0.0007	40.091[4]	0.002
M140	Ol.-free neph.	S	0.703410[2]	0.000006	0.512800[2]	0.000004	-	-	-	-	-	-
PN8	Ol.-free neph.	S	0.703269[3]	0.000008	0.512858[3]	0.000006	20.2067[3]	0.0008	15.6645[3]	0.0007	39.957[3]	0.002
J7	Tephrite	NC	0.703333[3]	0.000008	0.512891[3]	0.000006	19.1695[3]	0.0007	15.5792[3]	0.0007	39.085[3]	0.002
M56	Bas. trachy-and.	NC	0.703280[3]	0.000006	0.512890[2]	0.000004	-	-	-	-	-	-
FL426	Phonolite	S^C	-	-	0.512848[4]	0.000004	19.7492[4]	0.0009	15.6219[4]	0.0008	39.588[4]	0.003
M123	Tephriphonolite	NC	0.703310[2]	0.000006	0.512880[2]	0.000004	-	-	-	-	-	-
FL442	Phonolite	S^C	0.703198[3]	0.000006	0.512871[3]	0.000006	19.6438[3]	0.0004	15.6084[3]	0.0003	39.487[3]	0.001
M58	Phonolite	NC	0.703410[2]	0.000006	0.512870[2]	0.000004	-	-	-	-	-	-
PN7	Phonolite	S	-	-	0.512834[4]	0.000004	20.3548[4]	0.0006	15.6775[4]	0.0006	40.075[4]	0.002
PN11	Phonolite	NC	0.703263[3]	0.000006	0.512899[3]	0.000004	19.3220[3]	0.0007	15.5964[3]	0.0007	39.215[3]	0.002